Astronomy & Astrophysics manuscript no. ms
September 18, 2014
© ESO 2014

arXiv:1409.4788v1 [astro-ph.GA] 16 Sep 2014

Origin and z–distribution of Galactic diffuse [C II] emission

T. Velusamy and W. D. Langer⋆

Jet Propulsion Laboratory, California Institute of Technology, 4800 Oak Grove Drive, Pasadena, CA 91109, USA
e-mail: Thangasamy.Velusamy@jpl.nasa.gov

Received 11 June 2014 / Accepted 04 September 2014

ABSTRACT

Context. The [C II] emission is an important probe of star formation in the Galaxy and in external galaxies. The GOT C+ survey and its follow up observations of spectrally resolved 1.9 THz [C II] emission using *Herschel* HIFI provides the data needed to quantify the Galactic interstellar [C II] gas components as tracers of star formation.
Aims. We determine the source of the diffuse [C II] emission by studying its spatial (radial and vertical) distributions by separating and evaluating the fractions of [C II] and CO emissions in the Galactic ISM gas components.
Methods. We used the HIFI [C II] Galactic survey (GOT C+), along with ancillary H I, ^{12}CO, ^{13}CO, and C^{18}O data toward 354 lines of sight, and several HIFI [C II] and [C I] position-velocity maps. We quantified the emission in each spectral line profile by evaluating the intensities in 3 km s^{-1} wide velocity bins, "spaxels". Using the detection of [C II] with CO or [C I], we separated the dense and diffuse gas components. We derived 2-D Galactic disk maps using the spaxel velocities for kinematic distances. We separated the warm and cold H_2 gases by comparing CO emissions with and without associated [C II].
Results. We find evidence of widespread diffuse [C II] emission with a z–scale distribution larger than that for the total [C II] or CO. The diffuse [C II] emission consists of (i) diffuse molecular (CO faint) H_2 clouds and (ii) diffuse H I clouds and/or WIM. In the inner Galaxy we find a lack of [C II] detections in a majority (∼62%) of H I spaxels and show that the diffuse component primarily comes from the WIM (∼21%) and that the H I gas is not a major contributor to the diffuse component (∼6%). The warm-H_2 radial profile shows an excess in the range 4 to 7 kpc, consistent with enhanced star formation there.
Conclusions. We derive, for the first time, the 2-D [C II] spatial distribution in the plane and the z–distributions of the individual [C II] gas component. From the GOT C+ detections we estimate the fractional [C II] emission tracing (i) H_2 gas in dense and diffuse molecular clouds as ∼48% and ∼ 14%, respectively, (ii) in the H I gas ∼18%, and (iii) in the WIM ∼21%. Including non-detections from H I increases the [C II] in H I to ∼ 27%. The z–scale distributions FWHM from smallest to largest are [C II] sources with CO, ∼130 pc, (CO-faint) diffuse H_2 gas, ∼200 pc, and the diffuse H I and WIM, ∼330 pc. CO observations, when combined with [C II], probes the warm-H_2 gas, tracing star formation.

Key words. ISM: Diffuse gas — ISM: Warm Ionized Medium — Galactic structure: [C II] emission

1. Introduction

Ionized carbon is widespread throughout the interstellar medium (ISM) ranging from the tenuous warm ionized medium (WIM) component to the diffuse atomic and/or molecular hydrogen clouds, and the photon dominated regions (PDR) surrounding dense molecular clouds. Thus the 1.9 THz (158 μm) $^2P_{3/2}$–$^2P_{1/2}$ transition of C^+ ([C II]) is a very important tracer and diagnostic of ISM conditions. It is the strongest Galactic far-IR emission line and, under most conditions where carbon is ionized, is the most important coolant. The [C II] emission in the ISM can be excited over a wide range of interstellar environments through collisions with electrons, as well as atomic and molecular hydrogen (cf. Goldsmith et al. 2012; Wiesenfeld & Goldsmith 2014). Thus [C II] is a key tracer of the evolution of the largely atomic regions into denser, cooler, molecular clouds in which new stars are formed, and it is widely used as a tracer of star formation in the Milky Way and other galaxies (e.g., Malhotra et al. 2001; Contursi et al. 2002; Stacey et al. 2010; Braine et al. 2012; Pineda et al. 2014). The use of [CII] as a probe of galaxy evolution is growing in importance on all distance scales from the Milky Way to the highest redshift galaxies even to the epoch of re-ionization (e.g., Gong et al. 2012).

There is, however, an ongoing controversy about the origin of the bulk of the [C II] emission, which has been claimed to come primarily, or collectively, from the extended low-density warm interstellar medium (ELDWIM; Heiles (1994); Abel (2006)), the atomic gas (Bennett et al. 1994), and the photon-dominated region of molecular clouds associated with massive young stars (Shibai et al. 1991; Stacey et al. 2010). Almost all of these assertions were based on spectrally unresolved [C II] surveys of the ISM, whereas only a spectrally resolved survey can locate the source of the emission with which to evaluate the relative importance of each of these ISM components throughout the Galaxy. To date the *Herschel* Open Time Key Programme: Galactic Observations of Terahertz C+ (GOT C+) is the only spectrally resolved [C II] survey of the Galaxy that can be used to locate and quantify the various ISM contributions to the observed [C II] intensity (cf. Langer et al. 2010; Velusamy et al. 2010). The GOT C+ data are available in the *Herschel* data archives[1]. In this paper we use this data base to address the question of the origin of [C II] emission and its distribution throughout the Galactic plane, including its radial and vertical distributions and the diffuse component. We also use the [C II] and

⋆ *Herschel* is an ESA space observatory with science instruments provided by European-led Principal Investigator consortia and with important participation from NASA.

[1] ftp://hsa.esac.esa.int/URD_rep/GOT_Cplus/

CO gas fractions to derive the radial distribution of the warm-H_2 gas, which can be regarded as a measure of the star formation rate (SFR) and/or star formation efficiency (SFE).

Earlier Galactic surveys lacked the spectral resolution to resolve the velocity features needed to study such a wide range of ISM components. For example, the COBE-FIRAS all-sky map of the Galaxy in [C II] had a 7° beam and velocity resolution ~1000 km s^{-1} (Bennett et al. 1994), and the BICE map, though with better angular resolution of 15′ and velocity resolution of 175 km s^{-1}, covered only the limited Galactic longitude range $350° < l < 25°$ (Nakagawa et al. 1998). In contrast, the observations by FILM (Shibai et al. 1996) covered 360° in longitude and latitude to b=±60°, but only surveyed a narrow strip along a great circle. However, FILM with its ~12′ beam had a velocity resolution ~750 km s^{-1} that was insufficient for resolving spectral features. Thus in the post-*Herschel* era observations with GOT C+ and its follow-up, HIFI maps of [C II] along a number of strips remain the most valuable data set for characterizing the [C II] emission in the Galaxy. Unlike the [C II] emission from bright PDRs with high density and/or UV fields, which can be easily identified with their association with dense CO molecular clouds (with or without star formation) and, in some cases, with H II regions, the [C II] emission from the WIM and the diffuse atomic and molecular hydrogen gas are more difficult to separate because there is no convenient widespread ancillary tracer to distinguish them.

In the IRTS/FILM survey, Shibai et al. (1996) detected a dominant component that is highly concentrated within the Galactic plane with weaker [C II] emission slowly decreasing with Galactic latitude b beyond ~ 5° to 10°. Makiuti et al. (2002) conclude that the major source of the [C II] line emission observed by IRTS/FILM at high Galactic latitudes is the WIM. However, the data and the interpretation for the high latitude diffuse [C II] emission seen by COBE (cf. Bennett et al. 1994; Heiles 1994) and FILM (Makiuti et al. 2002) only apply to the local ISM (within a kpc in the solar neighborhood) and are not at all representative of the inner Galaxy. Little is known about this diffuse [C II] component in the inner Galactic disk. In this paper we use the GOT C+ survey of [C II] to separate its diffuse component using a statistical approach to identify characteristics that indicate the likeliest source of emission.

To date the GOT C+ data has been used in four major analyses (i) Pineda et al. (2013) used a globally integrated approach to separate [C II] emission components looking at the average properties as a function of Galactocentric radius, but limited to b=0° (ii) Langer et al. (2010, 2014b) and Velusamy et al. (2010, 2013) took a statistical approach to study the [C II] components arising from the CO-dark H_2 gas using the [C II] clouds identified in Gaussian fits to the narrow (< 8 km s^{-1}) spectral line profiles (iii) Velusamy et al. (2012) analyzed weak broad [C II] emission arising from the WIM along a spiral arm tangency, and (iv) Pineda et al. (2014) studied the [C II] radial luminosity as a tracer of Galactic star formation using only the b=0° data. In this paper we take a different approach that utilizes all the available [C II] detections and non-detections in the GOT C+ data base and (i) separates out the dense and diffuse ISM contributions to [C II] emission (ii) determines their spatial distribution throughout the inner Galactic plane and (iii) the distribution in z of each ISM [C II] component.

A common feature seen in the GOT C+ [C II] velocity profiles are a low brightness diffuse component in addition to the bright features associated with denser molecular clouds as traced by CO. The broad [C II] line wings are seen in the vicinity of much narrower emission features, which are often associated with CO counterparts. Some narrow line width features are possibly associated with diffuse H_2 without CO. However, a detailed study of this diffuse emission requires the ability to separate the diffuse [C II] emission from the dominant molecular gas component, thereby identifying all features within the spectral line profiles. These widespread low brightness broad [C II] velocity features are indicative of large-scale Galactic diffuse [C II] emission. Velusamy et al. (2012) used a subset of the data along the tangent Scutum-Crux spiral arms tangency, where path lengths are long and the [C II] emission has broad linewings extending beyond the tangential velocities, to conclude that the widespread [C II] emission came from the warm ionized medium (WIM).

Our primary objective in this paper is to understand how well [C II] traces the Galactic gas components: molecular H_2, atomic H I, warm neutral medium (WNM), and ionized (WIM); and then quantify what fraction of the total Galactic [C II] intensity traces each of these gas components. Here the [C II] intensity fraction in H_2 refers to the fraction of the total [C II] produced by ŧ excitation by H_2 molecular gas. For this purpose we include all H_2 gas components, that is both the dense and diffuse molecular clouds associated with and without CO emission. Our additional goal is to use the results of the [C II] gas components to derive their z–distribution. The Galactocentric radial distribution of the [C II] emission at b=0° has been well studied using the GOT C+ data (Pineda et al. 2013; Langer et al. 2014b) while less is known about its vertical z–distribution. (Note that in the rest of our paper we avoid using the term PDR for the H_2 molecular gas component of the [C II] emission. Though all molecular clouds are indeed PDRs as in photon dominated regions or photon dissociation/destructive regions, the use of the term "PDR component" is often misleading; for example Pineda et al. (2010, 2013) refers to the GOT C+ [C II] in dense molecular clouds which are traced by ^{13}CO as the PDR component.)

Our data consists of GOT C+ [C II] along with the ancillary H I, ^{12}CO, ^{13}CO, and C^{18}O spectra toward 354 lines–of–sight (LOS) in the inner Galaxy between l = 270° to 57°. However, rather than using Gaussian fitted individual [C II] spectral features (Langer et al. 2014b) or averaging azimuthally in rings (Pineda et al. 2013), here we adopt a different approach for analyzing the diffuse [C II] components. We calculate the intensities in 3 km s^{-1} wide bins over the entire extent of each spectrum. For each LOS starting with the H I spectral line profile, which has the widest velocity range, we divide the spectra into 3 km s^{-1} wide bins and compute the [C II], H I, and CO intensities in each bin. Each bin represents a unique volume in the Galaxy as specified by its V_{lsr} and the LOS position, hereafter we refer to these velocity bins as "spaxels". We then make a spaxel by spaxel comparison of the [C II], H I, and CO emissions to identify different ISM regimes. Because H I is widespread and easily detected throughout the Galaxy we use the H I spaxels to provide a measure of the spatial–velocity "volumes" in the Galaxy sampled for the statistical analysis. We evaluate the individual contributions from ISM gas components to the [C II] intensities using the spaxel statistics of [C II] detections with respect to CO and H I detections and intensities. Here we also provide additional evidence of the spatial structure of the diffuse emission using HIFI [C II] and [C I] longitude–velocity strip maps observed in another of our *Herschel* programs. The detection of [C II] emission in the CO clouds is indicative of the presence of a warm (T > 35 K) ŧ layer in them, while a non-detection of associated [C II] in CO clouds indicates too low a temperature to excite ŧ to a level that can be detected by GOT C+. Thus the warm H_2 gas is easily identified in the CO spaxel sample which traces the H_2 gas. We show how this simple combination of the [C II] and CO gas frac-

tions in the GOT C+ data provides a useful probe of the Galactic distribution of the warm-H_2 gas which is a measure of star formation.

We first determine correlations of the spaxel intensities (integrated over the spaxel velocity width of 3 km s^{-1}) of [C II], CO, and H I and then interpret them in terms of their association with dense molecular clouds, diffuse H_2 clouds, atomic H I clouds, or the diffuse WIM component. In addition to the GOT C+ data we present the results from our follow up HIFI mapping observations in [C II] and the fine–structure lines of carbon, [C I], to further support and confirm our conclusions regarding the contribution from the diffuse component. The spatial and velocity structure of the [C II] diffuse component is brought out clearly in these $l - V$ and $b - V$ maps obtained with HIFI cross scans (3′ to 24′ long) where [C I] emission is used as a tracer of molecular gas. Finally, we use the results of the [C II] gas components to derive their vertical z–distribution.

Our paper is structured as follows. The data is discussed in Section 2. In Section 3 we construct the spatial-velocity maps, and the results of the spaxel analysis, comparing the distributions of [C II] with H I and CO. In Section 4 we analyze the contributions of the ISM phases traced by [C II] and CO gas components with an emphasis on determining the sources of the diffuse [C II] emission. We also derive the radial profile of the warm-H_2 gas fractions which is useful as tracer of the star formation. In Section 5 we determine the z distribution of the sources of [C II], CO clouds, diffuse molecular hydrogen clouds, and the diffuse atomic and warm ionized medium (WIM). We also calculate the [C II] intensity fractions and in the inner Galaxy integrated in and above the plane, and use them to estimate the Galactic [C II] luminosity. We summarize our results in Section 6.

2. [C II] and ancillary data

The analysis in this paper uses the [C II] spectral line data from the GOT C+ survey (Pineda et al. 2013; Langer et al. 2014b), ancillary CO isotopologue and H I observations. In addition to these we use new [C II] and [C I], spectral line data from HIFI On-the-Fly (OTF) mapping observations presented here for the first time. We have chosen to use only the data for the inner Galaxy, as shown by a schematic representation in Figure 1, because this region of the GOT C+ survey has all the supporting observations. The spatial and velocity resolutions for each data set are summarized in Table 1. The spatial resolution in the HIFI OTF scan maps is coarser than that for pointed observations because of the undersampling used in this observing mode (see Section 2.2). Though the spatial resolutions for each data set vary significantly they do not affect the analysis and the results presented here. The [C I] (1-0) or CO intensities are not used for any quantitative comparison with [C II] intensities; instead, they are only used for assigning an identification to the [C II] emission of possible association with H_2 molecular gas. However, the H I intensities are used to estimate the [C II] originating in the H I cloud layers and the effects of their beam dilution are discussed in Section 4.3.2.

2.1. GOT C+ survey data

The [C II] data used in this paper are from the GOT C+ Galactic plane [C II] survey at 1900.5369 GHz taken with HIFI (de Graauw et al. 2010) on *Herschel* (Pilbratt et al. 2010). The GOT C+ [C II] and the ancillary ^{12}CO, ^{13}CO, and C^{18}O observations and data reduction are described in Pineda et al. (2013). In this paper we use the [C II] and CO data for 354 lines of sight toward the inner Galaxy in the longitude range l = 270° to 57° (see Figure 1). The corresponding H I data were extracted from the VGPS survey (Stil et al. 2006) for l =14° to 57° and SGPS (McClure-Griffiths et al. 2005) for l = 270° to 14°. The total of 354 LOS consist of 118 longitudes with 3 LOS at each longitude alternating between b = 0°, +0.5°, +1.0° and b = 0°, -0.5°, -1.0°. Note that although all the GOT C+ [C II] spectral line data used here were processed in HIPE 8, the HEB standing waves were fully corrected using standing wave shapes from off-source observations (see Pineda et al. 2013), an approach similar to that now available in HIPE 12. Our procedure is described in more detail on the Herschel Science

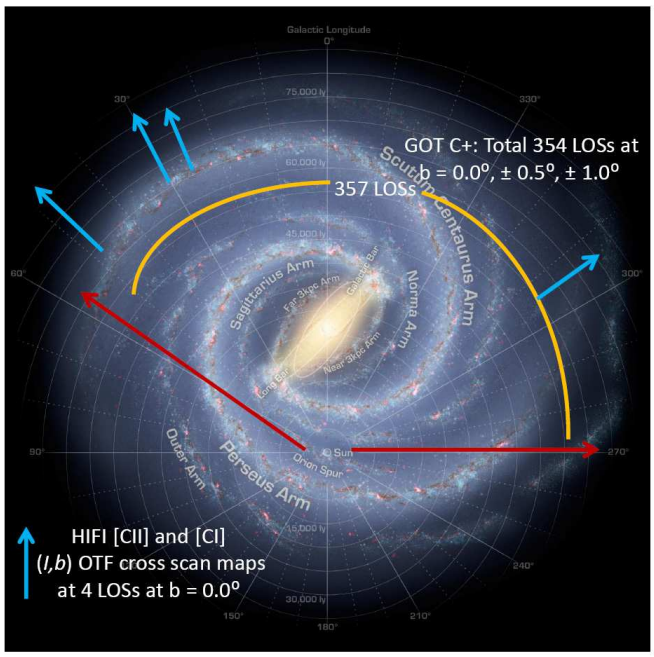

Fig. 1. Schematic showing the inner-Galaxy GOT C+ [C II] spectral line data (from KPOT_wlanger_1) and the HIFI cross-scan in (l, b) spectral line maps of [C II] and [C I] (from OT1_tvelusam_2). The red arrows define the longitudinal range of the GOT C+ data used here. The blue arrows show the longitudes for the 4 cross-scan maps presented here.

Table 1. Observational Data

Line	Data Facility	beam size	Velocity ΔV [km s^{-1}]	ref.
[CII] 1.9 THz	HIFI: GOT C+	12″ × 12″	1.0	1,2
	HIFI OTF			
	l-scan: 24′ long	80″ × 12″	2.0	1
	l-scan: 12′ long	40″ × 12″	2.0	1
	b-scan: 3′ long	20″ × 12″	2.0	1
[CI] (1-0)	HIFI OTF			
	l-scan: 24′ long	80″ × 46″	2.0	1
	l-scan: 12′ long	80″ × 46″	2.0	1
	b-scan: 3′ long	46″ × 46″	2.0	1
HI	SGPS/ATCA	132″	0.84	3
	VGPS/VLA	60″	0.84	4
^{12}CO (1-0)	ATNF/Mopra	33″	0.8	2
^{13}CO (1-0)	ATNF/Mopra	35″	0.8	2
^{13}CO (1-0)	FCRAO/GRS	45″	0.8	5

[1]This paper; [2]Pineda et al. (2010 and 2013); [3]McClure-Griffiths et al. (2005) [4]Stil et al. (2006); [5]Jackson et al. (2006);

Centre Website under the User Provided Data Products (herschel.esac.esa.int/UserProvidedDataProducts.shtml).

2.2. [C II] & [C I] HIFI Mapping Data

The [C II] and [C I] OTF scan mapping observations were taken with the HIFI instrument toward 13 selected GOT C+ LOS in the Galactic plane at b=0°. Here we present the results for only 4 LOS to demonstrate the presence of the diffuse [C II] in the position-velocity maps. These observations were taken between October 2011 and February 2012. At each LOS longitude the OTF spectral line cross-scan maps were made along the Galactic longitude and latitude. The longitude scan (l-scan) lengths vary between 3′ and 24′, as follows: 12′ (G030.0+0.0), 24′ (G045.3+0.0; G049.1+0.0; G0305.1+0.0; G345.7+0.0), and 3′ for the remaining 8 LOS. All 13 latitude scans (b–scans) are 3′ long. All HIFI OTF maps were made in the LOAD-CHOP mode using a reference off-source position about 2 degrees away in latitude. We used the off-source sky reference position from the GOT C+ program because we have knowledge there of any [C II] in the off-source spectrum. At each longitude the OTF scans were observed in three HIFI bands: [C I] (1–0) [$^3P_1$ – $^3P_0$] at 492.16065 GHz, [C I] (2–1) [$^3P_2$ – $^3P_1$] at 809.34197 GHz, ^{12}CO(7–6) at 806.6518 GHz, and [C II] [$^2P_{3/2}$ – $^2P_{1/2}$] at 1900.5369 GHz. For a 3′ OTF scan the typical observing times were ∼ 250s, 500s, and 2500s for [C I] (1–0), [C I] (2–1), and [C II], respectively. We used the Wide Band Spectrometer (WBS) with a spectral resolution of 1.1 MHz for all the scan maps. For the [C II] OTF observations the sampling was every 10″ over the 3′ scans, whereas we used 20″ and 40″ samplings for the longer 12′ and 24′ scans, respectively. The [C I] (1–0) scans were made with half beam (∼ 23″) sampling for all 3′ scans and 40″ sampling for the longer scans. The reconstructed images shown in Figs. 2 & 3 were restored with effective beam sizes corresponding to twice the sampling length along the scan direction, which accounts for the undersampling used for these OTF scans (Mangum et al. 2007).

The [C II] spectral line data were taken with HIFI Band 7 which utilized Hot Electron Bolometer (HEB) detectors. These HEBs produced strong electrical standing waves with characteristic periods of ∼320 MHz, that depend on the signal power. The HIPE Level 2 [C II] spectra show these residual waves. We found that applying the *fitHifiFringe*[2] task to the Level 2 data produced satisfactory baselines. However, removal of the HEB standing waves has remained a challenge up until the recent release of HIPE-12, which includes a new tool *HebCorrection*[3] to remove the standing waves in the raw spectral data by matching the standing wave patterns (appropriate to the power level) in each integration using a database of spectra at different power levels (see Herschel Science Center (HSC) HIPE-12 release document for details). We used this HSC script to apply *HebCorrection* to recreate the final pipeline mapping products presented here. Any residual HEB and optical standing waves in the reprocessed Level 2 data were minimized further by applying *FringeFit* to the "gridded" spectral data (we took additional precaution in *FringeFit* by disabling *DoAverage* in order not to bias the spectral line "window"). The H– and V–polarization data were processed separately and were combined only after applying *FringeFit* to the gridded data. This approach minimized the standing wave residues in the scan maps, as the standing wave differences between H– and V–polarization were fully taken into account. We found that in the [C II] maps produced with and without *HebCorrection* all the main features, including the diffuse low brightness emissions, were nearly identical. However, as expected, the noise level and baselines were better when we applied *HebCorrection*. Next we generated the l–V and b–V maps from the gridded spectral line data cubes, all created in HIPE 11 and HIPE 12 for [C I] and [C II], respectively. The matching l–V and b–V maps in H I were made for all LOS using the VGPS data. For a comparison of CO with the [C I] data we also produced l–V and b–V maps in ^{13}CO(1-0) for one LOS using the Galactic Ring Survey (GRS) (Jackson et al. 2006).

3. Results

3.1. Position-velocity maps and spectral line-wings: Evidence for diffuse [C II] emission

In this Section we present examples of position-velocity maps of several gas tracers that demonstrate the prevalence of a diffuse [C II] component. While [C II] emission arises from several gas environments, its association, or lack of association, with [C I] and CO identifies the likely ISM phase from which it arises. In Figures 2 we show an example of the longitude (12′) and latitude (3′) scan maps for l=30.0° and b=0.0° (labeled G030.0+0.0 in the figure). Though similar HIFI observations exist for several LOS, here we limit our study of these maps in order to highlight the position-velocity structure of the [C II] diffuse component and that associated with [C I] and CO. Detailed discussions of the individual features in these and other map data will be presented elsewhere. It can be seen in Figure 2 that there are differences in the spatial and velocity structure among the [C II], [C I], CO, and H I emissions. The spectral line intensities are shown in color scale (with color stretches indicated by the wedges) with longitude along the Y-axis and velocity (V_{lsr}) along the X-axis. The strongest emissions are seen near the tangential velocities (marked by the dashed vertical line) corresponding to the longest path lengths through the spiral arm.

As seen in Figure 2, there is an excellent correspondence between the HIFI [C I](1–0) and the ^{13}CO(1–0) emission. This correspondence demonstrates that both lines trace the presence of H_2 gas equally well. Comparison of the spatial and velocity distributions of the [C II] emission with those of [C I] and ^{13}CO, however, clearly differentiates two sources of the [C II] emission, namely, (i) the H_2 gas layers around the dense shielded components traced by [C I] and ^{13}CO and (ii) a diffuse gas component which is not traced by [C I] or ^{13}CO. Therefore, we can use the HIFI [C I](1–0) data as a marker for H_2 gas, and [C I] has added importance as an indicator of whether there is H_2 present in the diffuse transition clouds in which there is no detectable CO. In Figure 3 we show more examples of the l– and b–scan maps at three other LOS. For clarity of the display in Figure 3 we only show HIFI [C II] and [C I](1–0) maps. In each panel the [C II] emission is shown as a color image while the [C I] is shown as contours overlaid on the [C II] image.

As can be seen in Figure 2, there is little correlation of the [C II] or [C I] with the large scale distribution of H I. In all our l–V and b–V maps toward 13 LOS (not shown) H I is widespread over a broad velocity range, whereas [C II] and [C I] are confined to a much narrower velocity range. An H I self-absorption (HISA) feature seen in this map is marked by the arrow in the top panel in Figure 2. This foreground H I absorption is clearly detected in emission in both [C I] and ^{13}CO, but there appears to be

[2] http://herschel.esac.esa.int/hcss-doc-12.0/index.jsp#hifi_um:hifium section 10.3.2

[3] http://herschel.esac.esa.int/hcss-doc-12.0/index.jsp#hifi_um:hifium section 10.4.5

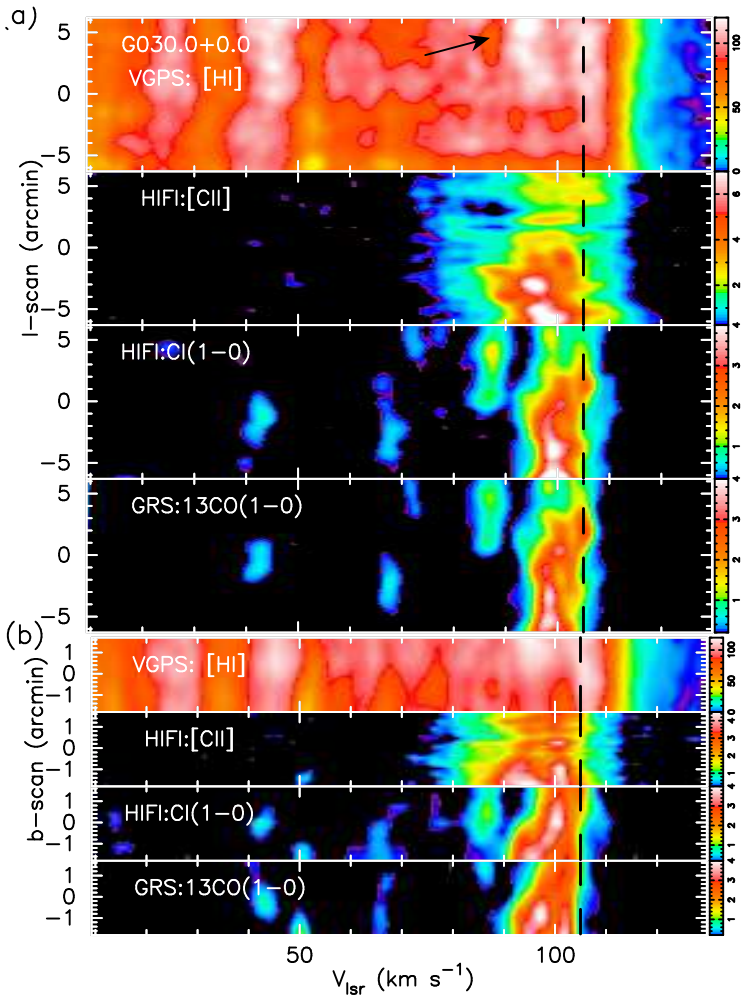

Fig. 2. Examples of *l*–*V* and *b*–*V* maps in H I, [C II], [C I], and ^{13}CO emission for LOS G030.0+0.0: (a) *l*–*V* maps; and, (b) *b*–*V* maps. The *l*–scans are at *b*=0°; *b*–scans are at *l*=30.0°. The intensities are in main beam antenna temperature (T_{mb}) with values indicated by the color wedges. These show low brightness diffuse [C II] emission along with the brighter narrow velocity features. Comparison of the spatial and velocity structures in the [C II] maps with those of [C I] and ^{13}CO delineates the [C II] arising from the denser H_2 molecular gas from the diffuse component. The vertical dashed line represents the tangential velocity for these regions. The velocity resolution in all maps is 2 km s^{-1}. The spatial resolutions are given in Table 1. The black arrow in the top panel marks an H I self-absorption (HISA) feature.

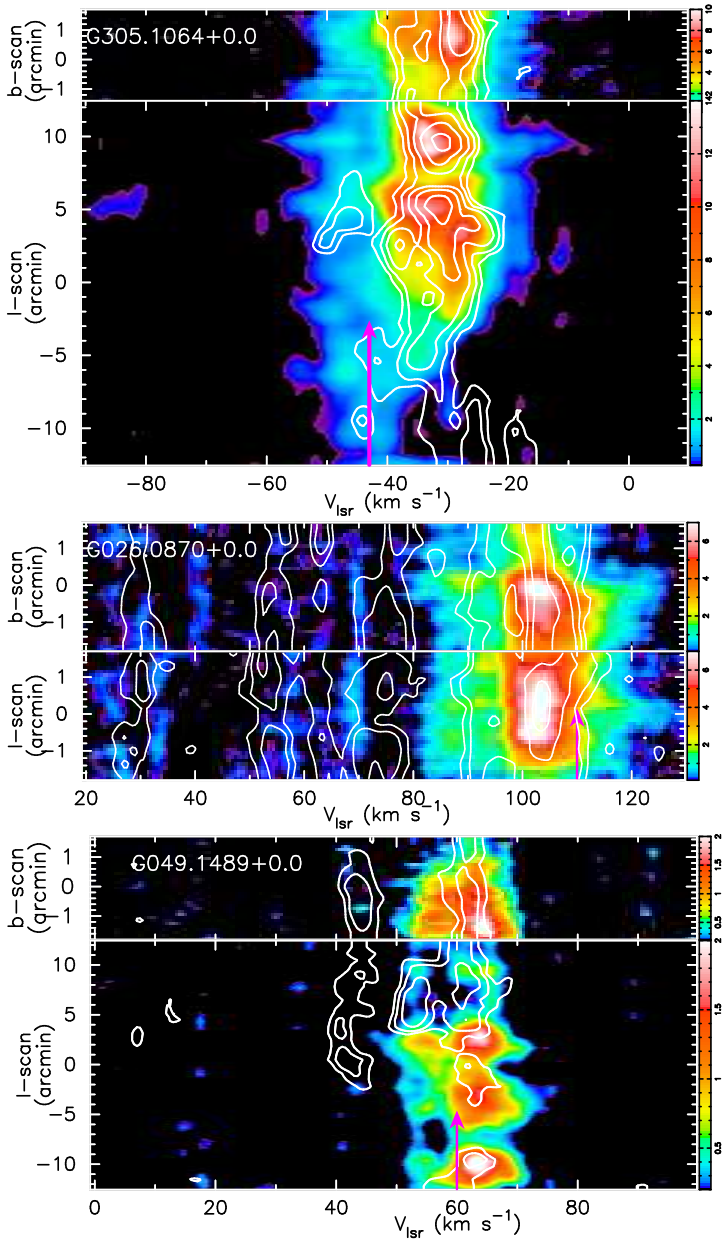

Fig. 3. Examples of (*l*–*V*) and (*b*–*V*) cross scan maps of [C II] and [C I] along 3 LOS: G305.1+0.0 (upper panels), G026.1+0.0 (middle panels), and G049.1+0.0 (lower panels). The *l*–scans are at *b*=0°; *b*–scans are at corresponding longitudes given in the images. The [C II] emission (in units of main beam antenna temperature, T_{mb}) are displayed in color with values indicated by the color wedges. The [C I] emission (T_{mb}) contours are overlaid on the [C II] maps, and their contour values are 0.2, 0.4, 0.8, 1.6 and 3.2 K. These maps show the low brightness diffuse [C II] emission along with the brighter narrow velocity features. The maps are centered at the indicated longitudes in each panel. The [C I] contours identify the underlying [C II] emission as those associated with the denser H_2 molecular gas, while [C II] emission without associated [C I] indicates a diffuse gas component. The vertical arrows mark the tangential velocities for each region.

a weak absorption feature in [C II]. The presence of absorption in the foreground cloud indicates that the excitation temperature of ɟ is low, implying a low T_{kin} and/or density. In Figures 2 and 3 all emission features show enhancement near the tangent velocities, largely due to the longer path lengths (Velusamy et al. 2012). At velocities beyond the tangent velocity no CO or [C I] is observed but both H I and [C II] show significant emission.

The images and contours in Figures 2 and 3 bring out the similarities and differences between [C II] and [C I] (as a proxy for CO) spatial and velocity structures. The *l*–*V* and *b*–*V* maps in Figures 2 and 3, as well as those for the other LOS, show the following characteristics of [C II] in relation to the spatial and velocity structure of the [C I] emission:

– H I has emission over the widest velocity range with only a small velocity range overlapping [C II] and/or [C I];
– [C I] emission has a relatively narrower velocity range than [C II];

– [C II] shows bright narrow velocity features roughly coincident with those in [C I];
– the broad angular and velocity extent of diffuse low surface brightness [C II] components are prominent in all maps;
– several [C I] features without [C II] counterparts are also present in the maps and these probably represent extremely low excitation conditions in the molecular clouds in which ‡, although present, is insufficiently excited to radiate (at the sensitivity of HIFI maps).

As can be seen in these figures there is a significant fraction of [C II] emission in the diffuse component and this result raises the question of what is the nature of the diffuse [C II] component of the ISM. Does it come from the cold neutral medium (CNM), the warm neutral medium (WNM), or the warm ionized medium (WIM), or some combination of these sources? We examine this question in Section 4.3 by estimating in the GOT C+ data how much [C II] emission is in (a) diffuse (CO faint) H_2 gas, (b) H I gas, and (c) the WIM.

The examples of the spatial–velocity maps in Figures 2 and 3 show the prevalence of the diffuse [C II] emission which can be seen (i) in position–velocity maps (*l*-*V* & *b*-*V* maps) as extended both spatially and in velocity and (ii) as broad wings in single spectral line profiles in the GOT C+ survey (see Figure 4). In this paper we use the spatial maps only for demonstration purposes to highlight the presence of the diffuse [C II] component. For all quantitative analysis we use the spectral line profiles in the GOT C+ data. The evidence for a significant fraction of [C II] arising in a diffuse component, as seen in the spatial–velocity maps, is also abundantly clear in the intensities of the [C II] line-wings. In Figure 4 we show examples of [C II] line profiles at five LOS in the inner Galaxy. In Figure 4 we also show the ^{12}CO line profiles to help delineate the broader line wings of [C II]. The line wings marked in panels (a) and (c) in Figure 4 can be traced as extended diffuse emission in the *l*–*V* maps shown in Figures 2 and 3. Thus the large (354 LOS) sample of GOT C+ spectra offer an opportunity to examine in great detail the diffuse component both in and out of the plane (at b=0.0°, b =±0.5°, and b =±1.0°), and provides much better statistics to compare the [C II] diffuse component with H I than the limited OTF map data. A detailed comparison of H I with both [C II] and CO helps us resolve the question of the fraction of [C II] originating from H_2 gas, diffuse H I, and the WIM.

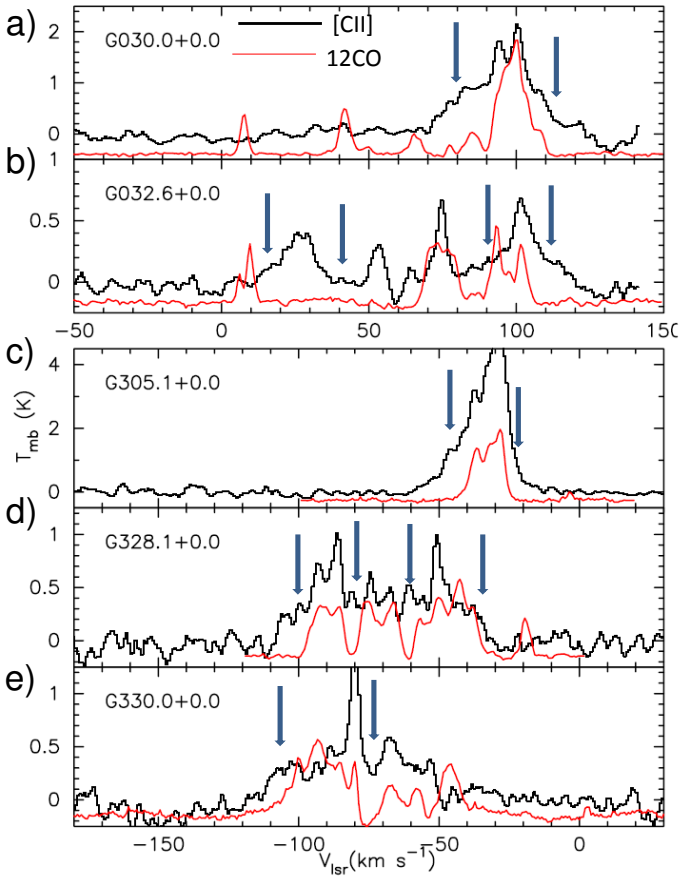

Fig. 4. Shown here are examples of broad line wings observed in GOT C+ spectra indicating the presence of a diffuse [C II] component. To help identify the [C II] associated with H_2 gas the ^{12}CO spectral line profiles are also shown. Only the [C II] intensities are labeled and CO intensities are scaled down arbitrarily to fit under the [C II] profiles. The line wings (diffuse [C II] components) are indicated by arrows. See also the corresponding *l*–*V* maps in Figures 2 and 3 for panels (a) and (c) which show the spatial extent of the line-wings (diffuse components).

3.2. Statistical approach of spaxel analysis

In this paper we analyze the statistical properties of an ensemble of spaxels to separate the contributions from the different [C II] components. To illustrate this approach we consider in detail one of the LOS [C II] spectrum along with all the ancillary H I and CO spectra, as shown in Figure 5. One can see that H I covers the entire velocity range shown, while ^{12}CO and ^{13}CO are more narrowly confined and [C II] covers a broader range than CO, but less than H I. To generate the spaxel data for this LOS we calculate the intensities in 3–km s^{-1} wide bins and identify those bins that have a minimum 3-σ detection. Along this LOS we now have ~65 of the 3–km s^{-1} spaxels, which we sort by whether they contain various combinations of gas tracers. We use these combinations to quantify the nature of the detections in each spectral line.

The results of the spaxel analysis of all LOS are summarized in Table 2, where we list the number of spaxels containing detections of the different gas tracers for all LOS. Note that a majority of the spaxels with the H I detections do not have [C II] and/or CO detections. As discussed in Pineda et al. (2013), while H I emission extends much further out in the Galaxy, [C II] and CO emissions are confined to the inner Galaxy within Galactocentric radius R_G < 10 kpc. Therefore we expect that a large number of spaxels with H I, but no [C II] or CO, (see Figures 6 and 7 below), are likely to be located at $R_G > R_\odot$ (=8.5 kpc) and to keep our sample homogeneous they should be excluded for all statistical interpretation of the H I and [C II] intensities.

3.2.1. Spaxel distances

The velocity resolved spectral data provide kinematic distances to each spaxel. We can also use this information to derive the *z*–distribution of the ISM gas components, which is important for determining the Galactic [C II] luminosity (see Pineda et al. 2014). We derive the distances to each spaxel from its V_{lsr} using a rotation curve based on the hydrodynamical models of Pohl et al. (2008) following the procedure discussed by Johanson & Kerton (2009) and using the code given to us by C. Kerton (private communication). This approach provides a more accurate kinematics of the clouds near the Galactic cen-

Table 2. Summary of the spaxel analysis of spectral line profiles

Item	Total	H I† Detections with			[C II] Detections		^{12}CO Detections		^{13}CO
	H I	[C II]	^{12}CO	[C II] and CO	total	with CO	^{12}CO	with [C II]	
3–σ detection limit K km s^{-1}	7.0	7.0	7.0	7.0	0.5	0.5	3.0	3.0	0.5
All data (354 LOS)									
Total No. of spaxels	23229	6484	4421	2705	6484	2705	4421	2705	3653
Intensity (K km s^{-1})	3336	1501	1117	794	10317	5811	61549	43236	8159
Spaxels with R$_G$ < 8.5 kpc									
Total No. of spaxels	15278	5711	4197	2609	5711	2609	4197	2609	3448
at b = 0.0°	5198	2356	2096	1388	2356	1388	2096	1388	1792
at b = ±0.5°	5363	1948	1340	826	1948	826	1340	826	1078
at b = ±1.0°	4717	1407	761	395	1407	395	761	395	578
Intensity (K km s^{-1})									
Total	2524	1377	1059	765	9132	5501	58790	41979	7807
at b = 0.0°	985	637	548	422	4272	3006	31913	23170	4361
at b = ±0.5°	883	465	338	239	2966	1692	18082	13273	2443
at b = ±1.0°	656	275	173	103	1894	803	8795	5536	1004
Spaxels without distance ambiguity (used for z–distribution)									
Total No. of spaxels	11738	4484	3380	2162	4484	2162	3380	2162	2854
Intensity (K km s^{-1})	1918	1098	868	644	7425	4629	49369	35773	6722

†All H I intensities are in units of 10^3 K km s^{-1}.

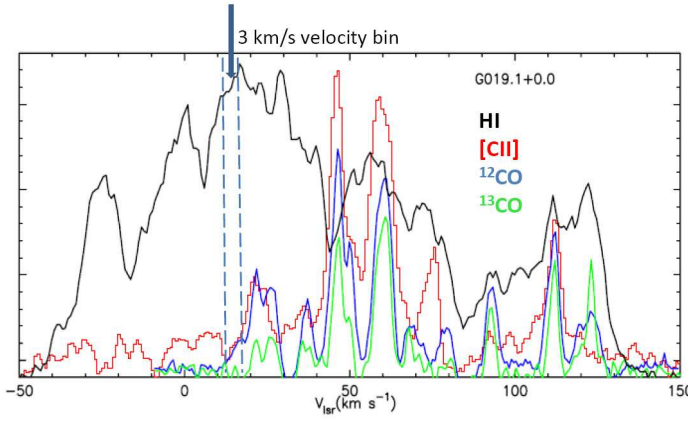

Fig. 5. An example of the GOT C+ spectral line data and spaxel analysis of [C II], H I, and CO spectra toward l = 19.1304° and b = 0.0°. Each "spaxel" corresponds to a 3–km s^{-1} wide velocity bin, as indicated schematically by the downward arrow and delineated by the dashed lines. The intensity scales for the spectra are not shown.

ter and thus more realistic distances for the longitudes $|l| < 6°$ than that using a simple rotation curve. In Figure 6 we show examples of [C II] and H I spectra for two LOS (l = 2.6° and 331.7°) showing the spaxel range V_{lsr} along with the derived V_{lsr} distance plots for Galactic rotation with and without a gas-flow model component. We assumed the rotation curve given by Johanson & Kerton (2009), the distance of the Sun from the Galactic center, R$_\odot$ = 8.5 kpc, and an orbital velocity of the sun with respect to the Galactic center, $V_\odot$ = 220 km s^{-1}. Thus for longitudes closer to the Galactic center the gas-flow model allows us to use all the observed velocity components, including those which are "forbidden" in a simple rotation curve. However, for $|l| > 6°$ there is little difference between the simple rotation and gas-flow models. We use the (V_{lsr}–Distance) plots obtained for each LOS longitude and then interpolate the distances for each spaxel V_{lsr} in the spectra. As indicated in the bottom panel of Figure 6 in all the LOS spectra, for a range of V_{lsr} corresponding to distances within the solar circle, the Galactic rotation models yield two solutions, a near– and a far–distance. However, each V_{lsr} represents a unique value for the Galactic radial distance (R$_G$). Therefore for any analysis that requires only R$_G$ we can use all the spaxels, and the number of spaxels detected within R$_G$ < 8.5 kpc are summarized in Table 2. For any other analysis that requires distances we use only the subset of spaxels for which we have unambiguous, or relatively high confidence, in their values and those for which the near– far–distance ambiguities can be resolved. Near the tangencies where the near– and far–distances are within 2 kpc we can use their average distances, thus these spaxel distances are good to within ±1 kpc.

Of the total of 15278 spaxels within R$_G$ < 8.5 kpc we have unambiguous distances for 3537 spaxels (~23%) located within 1 kpc of the tangency and another 1108 spaxels have unambiguous far–distance solutions. For the remaining 10633 spaxels, wherever possible, we use the H I self absorption (HISA) features in the H I spectra to resolve the distance ambiguity by following the procedure of Roman-Duval et al. (2009). Wherever H I absorption is detected at the spaxel V_{lsr} we adopt the near distance solution. The distances for spaxels without HISA detections are uncertain, and therefore, they are not used in our analysis. Examples of H I absorption features are indicated by the downward arrows in the top panel of Figure 6. Note that for illustrative purposes only a few selected dips are marked in the figure. Furthermore, only those dips which lie within the velocity range of the [C II] profile are relevant to our analysis. We identify the H I absorptions without bias using an IDL algorithm "EXTREMA" (Meron 1995). Thus we were able to place 6510 at the near–distance using the presence of H I absorption. Identifying HISA features requires care as it is probable that some of the identified H I absorption dips are not true HISA but represent some large scale feature. Likewise we may miss some of them due to beam smearing. It is difficult to assess individually the reality of all the HISA features. However because we are using a large ensemble in our analysis, the inclusion of a small fraction of spurious features will not affect our results in a significant way. Indeed, the fraction of HISA identified in our sample is consistent with the expectation for the frequency of HISA. For example, the fraction in our sample (~61%) is roughly consistent with the frequency of HISA in the sample

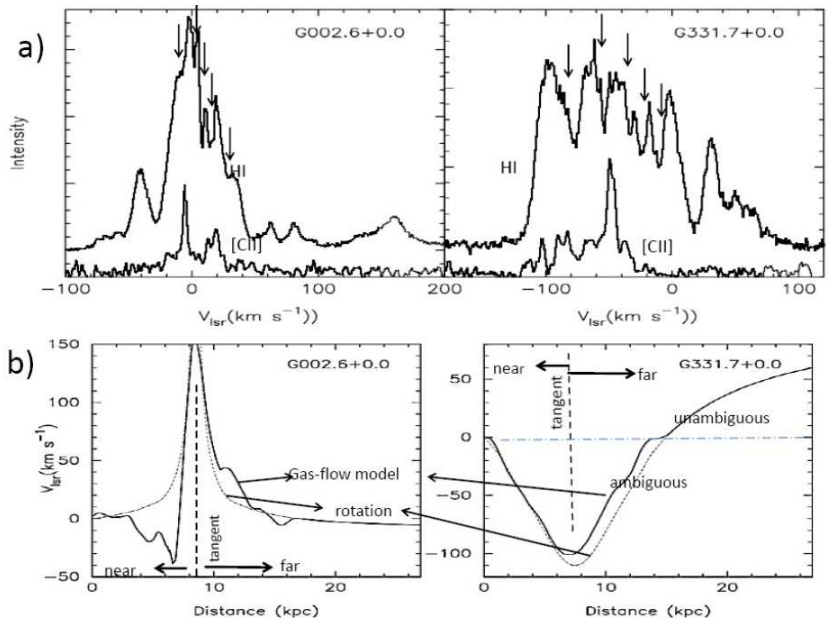

Fig. 6. (a) Examples of [C II] and H I spectra at two longitudes. The downward arrows over the H I velocity profiles represent the H I absorption features used to resolve the distance ambiguity (see text). The temperature scales for H I and CO are not indicated. (b) The V_{lsr} distance relation is shown for the longitudes of the spectra in panel (a). The dotted line represents the solution for a standard Galactic rotation model. The solid line represents that for standard Galactic rotation supplemented by the gas-flow model (see text). The vertical dashed line indicates the tangent distance.

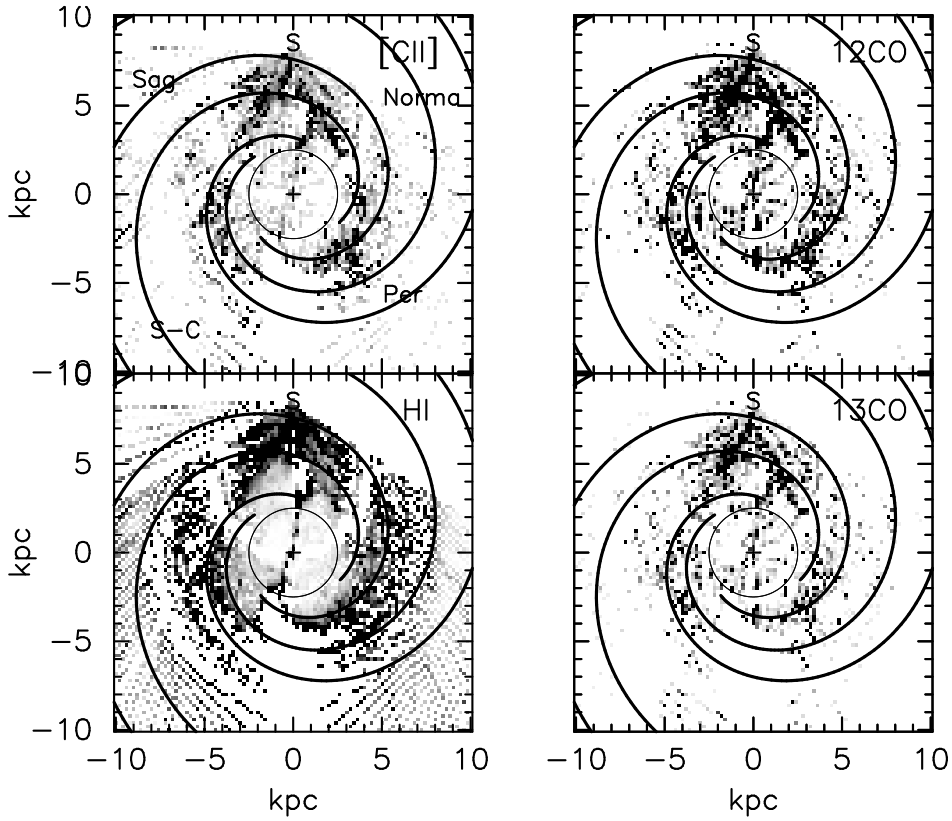

Fig. 7. 2-D maps of Galactic [C II] emission compared with that of H I and CO emissions in the spectral line data in the GOT C+ survey. Here we use all spaxels with distance estimates (see text). We use only intensities in the spaxels with H I, [C II], or CO detections. The spiral arms are identified in the top left panel and S denotes the solar system. The circle (2 kpc radius) marks the Galactic center region. The void seen near the tangent points in all maps is an artifact resulting from the algorithm used to resolve the near– far–distance ambiguity (see text).

used by Roman-Duval et al. (2009). In their survey of 702 ^{13}CO sources with near– and far–distance ambiguity they constrained the solutions to the near–distance for ~70% of the sources. For comparison, in our analysis of 3361 spaxels detected with ^{12}CO we constrain ~62% of them to the near–distance solution.

3.2.2. 2-D Galactic maps

We use the spaxel intensities and distances, in all latitude (*b*) data, to produce 2-D Galactic maps of four gas tracers. Figure 7 shows the maps of Galactic [C II] emission compared with H I and CO emissions derived from the intensities in the spaxel and using the radial velocity distances. For H I we use all spaxels, but for [C II] and CO we use only the spaxels with 3-σ detections. The logarithmic spiral arms (Vallée 2008; Steiman-Cameron et al. 2010) are plotted on the 2-D Galactic maps. Figure 7 is the first 2-D representation of the Galactic [C II] emission in the plane. We can see that most of the [C II] emission is closely associated with the spiral arms and it is brightest near the spiral arms' tangent points. In the Galactic intensity maps we can identify two major artifacts, both resulting from the V_{lsr}–Distance transformation. The first are the radial striations (or "fingers") caused by velocity dispersions (peculiar or streaming motions) that confuse the distance estimates resulting in a smeared radially elongated feature along the line of sight (cf. Levine et al. 2006; Englmaier et al. 2011). For example, the elongated strips near the Galactic center are likely to be caused by such velocity dispersions. The second are the voids seen near the tangent points in both longitude quadrants in all maps which are an artifact resulting from the algorithm used to resolve the near– far–distance ambiguity. In the V_{lsr}–Distance solution for spaxels with velocities close to the tangent velocity (Figure 6b) the far–distances, up to within 1 kpc from the tangent point, are assigned to the near–distance. Thus the lack of spaxels at distances up to 1 kpc beyond the tangent point results in the void seen in the maps. Furthermore, all spaxels with V_{lsr} exceeding the tangent velocity (due to peculiar or streaming motions) are set to be at the tangent distance, resulting in an accumulation of spaxels at the tangent points. However, the scale of the radial striations or the void (~1 kpc) is within the distance uncertainty assumed for the analysis and therefore do not change our results for *z*-scales derived using the kinematic distances. We do not discuss further the Galactic distribution of [C II] in the spiral arms because it can be studied better using the HIFI OTF scan maps observed from other *Herschel* programs. Another striking difference between [C II] and CO maps is the diminished [C II] emission within 2 – 3 kpc of the Galactic center. While CO surveys find strong emission in the center (cf. Dame et al. 2001), in the BICE [C II] data Nakagawa et al. (1995) reported a deficiency of [C II] toward the Galactic Center. While H I is detected to large radial distances covering the full extent of the map the [C II] and CO are not detected at radial distances much beyond the solar circle, which is consistent with the radial distributions reported in Pineda et al. (2013).

4. Analysis of the ISM phases traced by [C II]

In the previous sections we described a method to represent the [C II] survey statistically in terms of spaxels and discussed how we determine their location in the Galaxy. We summarize the details of the data used in our analysis in Table 2. We identified a total of 23229 spaxels (each with a 3 km s^{-1} wide velocity bin) in the GOT C+ data selected by their H I detections (3-σ = 7 K km s^{-1}). Of these only 6484 spaxels were detected in [C II] (3-σ = 0.5 K km s^{-1}) and 4421 in ^{12}CO (3-σ = 3.0 K km s^{-1}). Thus the vast majority (~72%) of H I spaxels do not have detectible [C II] emission, even though [C II] emission is expected to be associated with both H I and H_2 (the collisional excitation rate coefficient for exciting + is about 1.5 times larger for H atoms than H_2 (Wiesenfeld & Goldsmith 2014)). This statistical result on the association of [C II] emission with H I and CO raises the question, why is there such a low fraction of H I associated with [C II] emission, given the rather widespread distribution of H I throughout the Galaxy? Here we use the spaxel data set and the GOT C+ Gaussian fits (Langer et al. 2014b) to compare statistically their relationships and identify the origin of [C II] from different ISM components.

As seen in the intensity distribution maps in Figure 7, the spaxels at Galactocentric radii $R_G > R_\odot$ are dominant only in H I with little or no [C II] emission. Therefore, for a statistically significant comparison of the [C II] detections with H I it would be unrealistic to include the spaxel population at $R_G > R_\odot$, because it would bias the result. Therefore we exclude these from further analysis.

4.1. [C II], CO Detections: Galactic distribution and Comparison with H I

4.1.1. H I Intensities/Column densities

In Figure 8 we summarize the [C II] and CO spaxel detections as a function of H I intensity for the 15278 spaxels identified at $R_G < R_\odot$. In panel Figure 8(a) we display the fraction of spaxels with [C II] and CO detections as a function of H I intensity; this fraction is a measure of the detection rates of [C II] and CO in the Galaxy. The spaxel fractions for each H I intensity bin are defined as the ratio of number of spaxels with detections of a given gas component (e.g., [C II], [C II]-with-CO) to the total number of H I spaxels in the bin. Both [C II] and CO have higher detection rates at higher H I intensities (corresponding to higher H I column densities and/or local H-atom densities). The detection rates for [C II] spaxels associated with CO show a nearly identical increase with H I intensity as ^{12}CO with H I, whereas the [C II] spaxels without CO do not show any significant increase with H I intensity. To further examine the fraction of detections in Figure 8(a), we show in Figure 8(b) the number distribution of H I, [C II], and ^{12}CO spaxels as a function of H I spaxel intensity. We find that for $R_G < R_\odot$ a low fraction (~27%) of H I spaxels have CO detections and have an even lower fraction of [C II] with CO detections (~17%). We interpret this result as a consequence of the fact that only a small number of H I clouds are seen in association with dense H_2 gas. Although the [C II] detection rates, especially for those with CO, correlate well with the H I intensity, the [C II] intensities do not show any correlation with H I intensity (see Fig. 9 in Langer et al. 2014b) and show a large scatter (over two orders of magnitude). Therefore, we interpret the higher rate of detection at large H I intensities, not as arising from the H I gas itself, but with the probability for the presence of high density molecular gas associated with increasing H I column density. In other words, as H_2 fractions are expected to increase with increasing H I column densities (e.g., Sternberg et al. 2014) the likelihood of detecting H_2 excited [C II] emission also increases.

About 17% of the H I spaxels are associated with both [C II] and CO emission, while a similar fraction ~20% of the H I is associated with [C II] emission without CO. To understand better the statistics of H I versus [C II] emissions we show in Figure 8(c – e) the results for the GOT C+ LOS grouped by the absolute

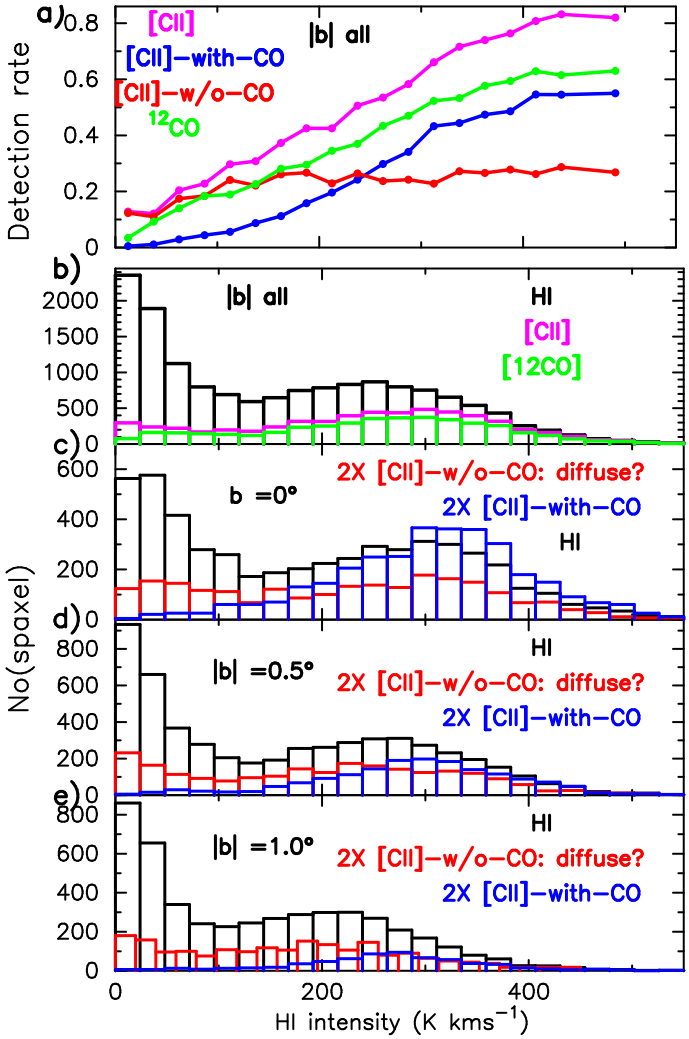

Fig. 8. Comparison of the gas components of [C II] emission as a function of H I intensity for Galactocentric radius $R_G < R_\odot$ (8.5 kpc); and for different values of *b* as indicated in panels (a) to (e) (see Table 2). (a) The fraction of detections of [C II] and ^{12}CO components and combinations of [C II] and CO (as indicated by the colors) plotted against H I intensity. (b) Histogram representation of the number distribution of spaxels detected in H I, [C II], and ^{12}CO as a function of H I intensity. (c) – (e) The number of [C II] detections compared with the H I intensity shown for each absolute value of the latitude separately. The [C II] detections with and without CO are plotted separately to bring out differences between the dense and diffuse components of [C II] emission.

value of Galactic latitude. Note that here we plot the latitudinal distributions for [C II] detections with and without CO separately to bring out the remarkable differences in their distribution in and out of the plane. We classify the [C II] detections in the spaxels as (i) "[C II]-with-CO": spaxels in which both [C II] and ^{12}CO emissions are detected, and (ii) "[C II]-w/o-CO": spaxels in which only [C II] is detected and no ^{12}CO emission is detected. The overall number distributions of spaxel detections in Figure 8 show:

– Figure 8(a): The detection fractions (defined as the ratio of the number of detections to the total number of H I spaxels in a given H I intensity bin) for [C II]-with-CO and ^{12}CO show similar increase with the H I intensity; however the detection fractions for [C II]-w/o-CO show little or no dependence on H I intensity.
– Figure 8(b): At intermediate and high H I intensity both the number of [C II] and CO detections (spaxels) show some degree of correlation with the total number of H I spaxels. However, at low H I intensity, their detection rate does not show any relation to the number of H I spaxels at any given intensity.
– Figure 8(c–e): At H I intensities >200 K km s^{-1} the number of [C II]-with-CO detections shows a stronger dependence on the number of H I spaxels than that for [C II]-w/o-CO. At lower H I intensities (<200 K km s^{-1}) the [C II] with or without CO detections are nearly independent of the number of H I spaxels in each intensity bin.
– Figure 8(c–e): [C II]-with-CO detections show a stronger dependence on Galactic latitude with the highest detection rates at b=0°, decreasing sharply as $|b|$ increases.
– Figure 8(c–e): In contrast to the [C II]-with-CO, the [C II]-w/o-CO detections have (i) a very similar number distribution in all three latitudes and (ii) show no dependence on the number of H I spaxels in each H I intensity bin.
– There is no apparent correlation between the [C II] and H I intensities in the spaxels with [C II] detections (see below).

In the following we use the results of the spaxel detection only to quantify the fraction of Galactic [C II] likely to be associated with H_2 gas (see Section 4.2) and to differentiate it from the emission in the diffuse atomic H I gas or the WIM (see Section 4.3). Here we do not calculate the amount of CO-dark H_2 in the FUV illuminated layers of CO clouds, which has already been analyzed in our earlier work (Langer et al. 2010; Velusamy et al. 2010, 2013; Langer et al. 2014b).

4.1.2. Galactic radial distribution

The radial distribution of gas tracers gives the global characteristics of the ISM in the Galaxy and are more robust without the ambiguity of the near– far–distance determination discussed above. The characteristics of the [C II] emission, including the CO-dark H_2 gas, as a function of Galactocentric radius, R_G, in the Galactic plane have been reported in previous GOT C+ publications (Pineda et al. 2013; Langer et al. 2014b). Here we present a slightly different perspective as revealed in our spaxel spectral analysis of the GOT C+ data. We use these Galactic radial distances of the spaxels and the spectral line detections in them to derive their distributions as a function of R_G. The spaxel data are binned in R_G in 0.5 kpc widths sampled every 0.5 kpc. We count the number of spaxel detections and their total intensities in each bin for H I, [C II], and ^{12}CO. In Figure 9a (upper panel) are shown the radial distributions of the number of detections of H I, [C II], and CO and in Figure 9a (lower panel) are shown the radial distributions of their individual gas components [C II]-with-CO, [C II]-w/o-CO, and CO-w/o-[C II].

The number of spaxels in each R_G–bin depends on the Galactic volume sampled. Because the GOT C+ survey does not sample the Galactic volume uniformly we need a "volume" normalization for each R_G–bin to interpret these distributions. We use the total number of H I spaxels in each R_G–bin for the normalization. As seen in the examples of the spectral line profiles of [C II] and all ancillary data in the GOT C+ data base (see Figure 5) the H I profile always has the broadest velocity range and encompasses all the emission features in [C II] and CO. In other words, all the [C II] and CO features lie within a, generally, broader H I emission profile as a function of velocity. Thus all

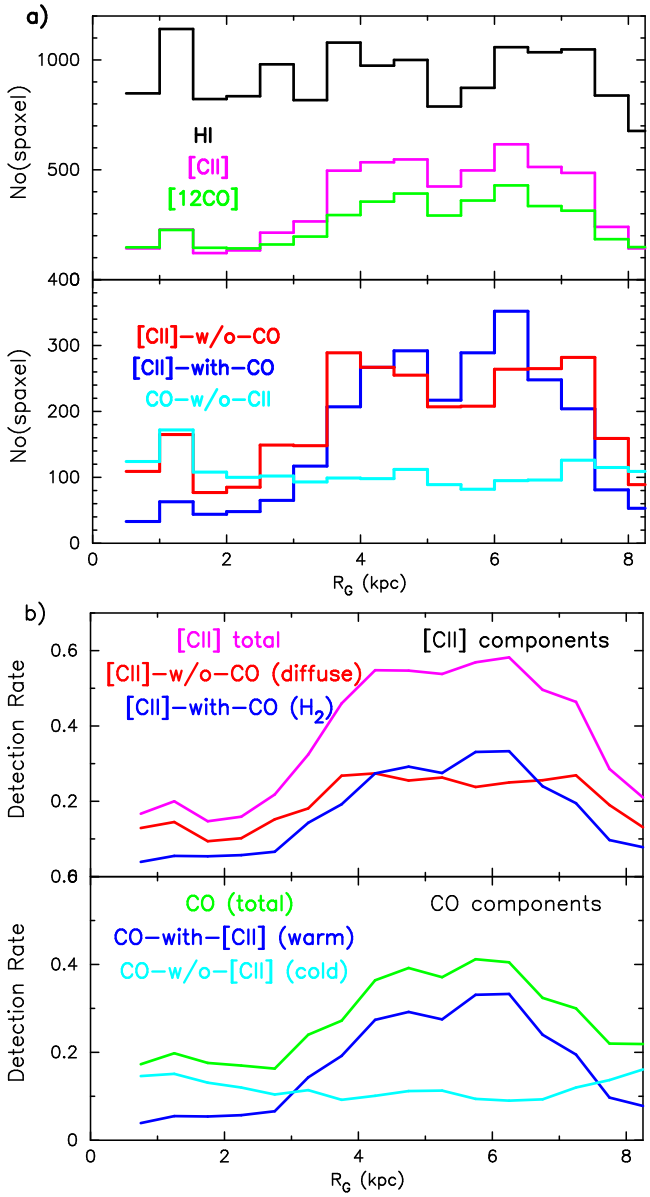

Fig. 9. Comparison of the ISM gas components as a function of Galactocentric radius R_G. The spaxels for $R_G < R_\odot$ (8.5 kpc) are the only ones used (see Table 2) for the analysis. (a) Histogram representation of the number distribution of spaxels detected in H I, [C II], and ^{12}CO as a function R_G (upper panel). Number of detections of the [C II] and CO components (lower panel) (b) Detection rates of [C II] (upper panel) and CO (lower panel) components (normalized using the number of H I spaxels in each R_G–bin as measure of the sampled volume) as function R_G.

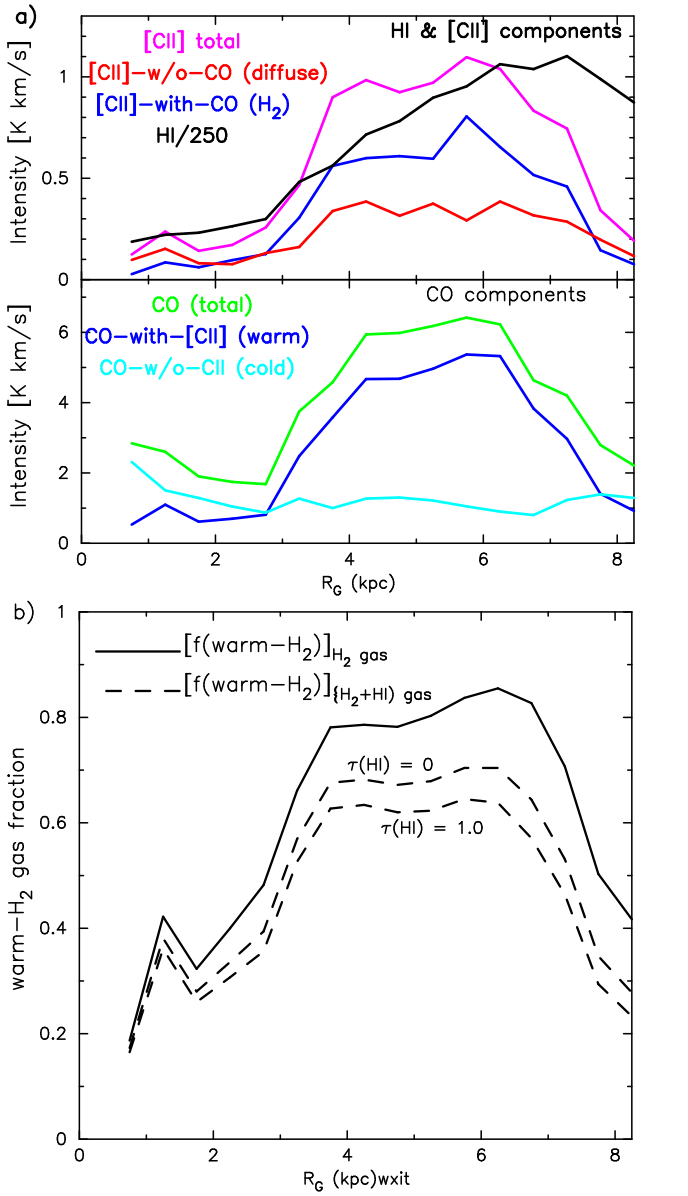

Fig. 10. (a) Radial distribution of the spectral line intensities (normalized using the number of H I spaxels in each R_G–bin as measure of the sampled volume) of H I, [C II] and its gas components (upper panel) and CO and its gas components (lower panel). (b) Galactic distributions of warm H_2 gas fraction, f(warm-H_2): (a) with respect to the total H_2 gas (solid line); (b) with respect to the total H I+H_2 gas (dashed line); τ(H I)=0 and 1.0 represent f(warm-H_2) for optically thin and thick cases used for H I column densities, respectively. The variation of the H_2 fractions as a functions of Galactocentric radius R_G are representative of the star formation rate (SFR) and star formation efficiency (SFE).

the spaxels in our sample have H I detections. We can therefore use the number of H I spaxels in a given R_G–bin to represent a measure of the Galactic volume sampled within that R_G–bin. We define the detection rates of [C II], CO and their gas components as the ratio of the number of detections in each R_G–bin of the respective gases to the total number of H I spaxels in the R_G–bin. In Figure 9b are shown the radial distributions of the detection rates, which are now free from the bin-to-bin variations in the sampling, of the various [C II] gas components (top panel) and CO gas components (lower panel).

We find that the [C II] detection rates peak in the range 4 kpc < R_G < 7 kpc. The [C II] with CO (the H_2 gas) is strongly peaked over this range of R_G, while [C II]-w/o-CO (the diffuse gas) has a shallower peak and a broader distribution in R_G. The radial distribution of CO is roughly similar to that of [C II] with a broad peak in the range 4 kpc < R_G < 7 kpc. *However, the CO gas components with and without associated [C II] emission show distinctly different radial distributions*. The CO emission spaxels without [C II] detections represent cold CO with H_2 gas clouds in which the C^+ layers are too cold for efficient excitation of the C^+ $^2P_{3/2}$ state. On the other hand the spaxels with detections of [C II]

along with CO represent H_2 clouds in which the C^+ layers are sufficiently warm (> 35 K) for efficient [C II] excitation. Thus the results in the lower panel in Fig. 9b delineate remarkably well the Galactic radial distributions of the warm–H_2 and cold–H_2 gas clouds. In contrast to the warm-H_2 broad peak in the range 4 kpc < R_G < 7 kpc, the cold-H_2 shows a flat and more uniform distribution at all R_G. Indeed there is even hint of a decrement in cold–H_2 near the peak of the warm–H_2 gas.

For quantitative analysis, as done above for the detection rates, we derive "volume" normalized intensities of [C II], CO and their gas components defined as the total spaxel intensities divided by the number of H I spaxels in each R_G–bin. In Fig. 10a are shown the radial distributions of the intensities per unit volume for H I, [C II] and its gas components (upper panel) and CO and its gas components (lower panel). These results are broadly consistent with those derived by Pineda et al. (2013) using the azimuthally integrated intensities and the geometric area of each annular ring. The results presented here provide a good representation of the non-uniform sampling within the annuli but normalized to arbitrary volumes that may differ from spaxel–to–spaxel. Thus, they bring out clearly, and provide additional confirmation of, the global [C II] and CO emission characteristics discussed by Pineda et al. (2013, 2014). Most importantly, the differences in the radial distributions for the cold and warm H_2–gas, as indicated by their association with or without [C II], raise the possibility of using the intensities as a measure of the star formation efficiency (SFE) and/or rate (SFR). Star formation will heat the gas and thus the warm clouds are signatures of recent star formation. The cold clouds, in contrast, are located in regions without recent star formation. Therefore by combining both [C II] and CO emission in the spaxel analysis along with H I, we have a measure of the SFR and/or SFE.

We assume that the CO intensities in the spaxels measure the H_2 column density (neglecting the CO-dark H_2 in the C^+ layer). Although the ^{12}CO emission is generally optically thick it has been shown that the intensity of ^{12}CO is proportional to the column density of H_2 of molecular clouds (see the recent review by Bolatto et al. 2013) and $N(H_2)=X_{CO}I(^{12}CO)$, where X_{CO} is the CO-to-H_2 conversion factor. While the cold–H_2 is found to be roughly uniform with R_G, the warm–H_2 is predominantly in the range 4 kpc < R_G < 7 kpc. The presence of warmer H_2 is an indication of a star formation environment. Thus, in Fig. 10(b) we plot the warm–H_2 gas fractions with respect to (i) the total H_2 gas (solid line) and (ii) total gas including H I (dashed lines). We use the H I and CO intensities in each R_G–bin to derive their column densities, N(H I) and $N(H_2)$. For H I column densities we consider optically thin ($\tau << 1$) and thick ($\tau = 1.0$) cases for the inner Galaxy (e.g., Kolpak et al. 2002) as marked in Fig. 10b. The H I column densities are corrected for the optical depth using Eq. 8 in Chengalur et al. (2013). Treating the presence of warm–H_2 as evidence for star formation we can relate the radial profile warm–H_2 gas fractions to that of the star formation rate and/or efficiency. The radial profiles of the warm–H_2 gas fractions with respect to total gas have a flat peak (value between 0.6 and 0.7) at R_G between 4 and 7 kpc. The star formation rate will depend on the star formation efficiency and the gas available to convert to stars, and the spaxel analysis used here provides an important constraint on the warm-H_2 gas fractions and thereby the radial profile of star formation in the Galaxy.

4.2. [C II]-with-CO emission tracing the dense H_2 gas

The apparent correlation of the [C II] detection rate with H I intensity in Figure 8(a) agrees so well with that for CO with H I, that we can, with confidence, partly attribute some of the [C II] emission to a dense H_2 gas component, and it is an indication that the [C II] does not originate primarily in the H I gas. It is further evident by the fact that at high H I intensities the detections of [C II]-with-CO show a similar dependence on H I intensity as CO, while that for [C II]-w/o-CO show little dependence on the H I intensity. This correlation shows that both [C II] and CO have higher detection rates at higher H I intensity, but their intensities do not correlate with H I intensity. This result can be interpreted as follows: the higher H I intensities mean higher H I column density within the spaxel volume, thereby, increasing the probability for the presence of H_2 gas in it. This is consistent with the fact that the H_2 gas fraction increases with H I column density (e.g., Braine et al. 2011, 2012; Sternberg et al. 2014). Thus we conclude that for all spaxels having [C II]-with-CO the significantly large [C II] is excited by H_2 gas, with only a small contribution coming from the H I layers (cf. Langer et al. 2014b)). We estimate the contribution from the H I layers as follows.

The H I column density N(H I) [cm^{-2}] in each spaxel, in the optically thin limit, is proportional to the H I intensity: N(H I) = 1.82×10^{18} I(H I) cm^{-2} where I(H I) is in units of [K km s^{-1}]. We derive the column density of $+$ from N(H I) using the procedure given in Langer et al. (2014b) [their Equation A5] and the assumptions therein, N($+$) = N(H I) $X_H(C^+)$ where $X_H(C^+)$ is the carbon abundance. Here we assume $X_H(C^+)$ ~2.2×10^{-4}, typical for the Galactocentric radii where most [C II] arises. Expressing the H I density and temperature in terms of a pressure (P = n(H I)×T_K K cm^{-3}) and H I intensity in the spaxel (I(HI) (K km s^{-1}) we can write the emission in the H I gas simply as,

$$I(CII)_{HI} = 1.03 \times [P/3000] \times [I(HI)/1000]\,[\mathrm{K\,km\,s^{-1}}] \qquad (1)$$

From the analysis above we conclude that all [C II]-with-CO detections, which trace the dense molecular clouds, are associated with H_2 gas, and that their H I layers make only a small contribution to the spaxel [C II] intensity. We compute the emission from the H_2 gas as $I([C\,II])_{H_2} = I([C\,II])_{total} - I(CII)_{HI}$. We estimate the contribution from H I gas, assuming a H I gas pressure, P ~ 5000 K cm^{-3} (corresponding to the median spaxel radial distance, R_G ~ 5.5 kpc (Wolfire et al. 2003; Pineda et al. 2013)). The fractional emission from these dense H_2 clouds is given later in the final summary in Figure 14.

4.3. [C II]-w/o-CO emission: as diffuse H_2, diffuse H I, or WIM?

It is evident in Figure 8(a,c–e) that for the [C II] detections with CO there is some correlation with H I intensity, whereas for those without CO there is no direct correlation with the number of H I spaxels or the H I spaxel intensity. Therefore, for the analysis of the diffuse [C II] emission we exclude all the spaxels with CO detections as they are definitely associated with the dense H_2 gas. Thus the [C II] detections in the spaxels without associated CO detections (designated as [C II]-w/o-CO) represent emissions originating in (i) diffuse H_2 gas with no CO (or diffuse CO–faint H_2 gas), (ii) H I clouds and (iii) the WIM.

4.3.1. Gauss fit data: (CO-faint) diffuse H_2 gas

An additional component of H_2 molecular gas which is missed by CO but detected in [C II] has been identified in the GOT C+ survey (cf. Langer et al. 2010; Velusamy et al. 2010; Langer et al. 2014b). This component represents an early phase of cloud evolution or a Galactic environment where little or no

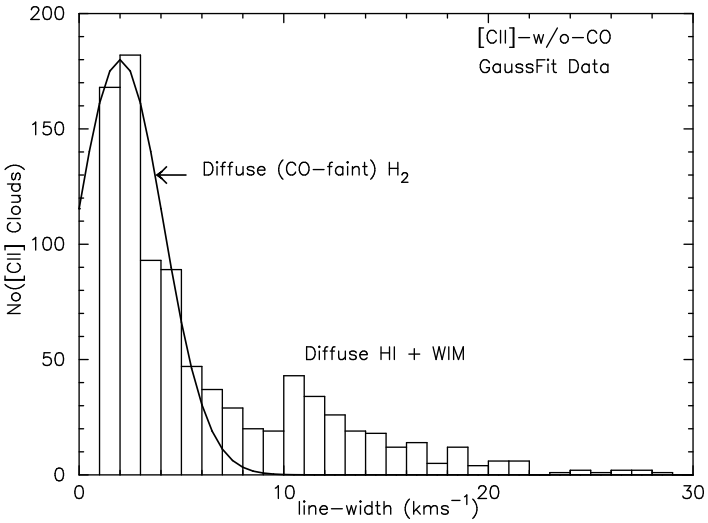

Fig. 11. A histogram of the Gaussian line widths of [C II] velocity components without CO in the GOT C+ data. The distribution is used to delineate the broader components, corresponding to low surface brightness extended emission arising from diffuse H I or the WIM, from the narrower line width associated with the diffuse molecular (CO faint) H_2 gas. The Gaussian line widths are taken from the data base assembled by Langer et al. (2014b).

CO exists because the gas is suffused with photodissociating UV radiation. Unlike the situation found for the spaxel data it is easier to identify such diffuse molecular clouds in the GOT C+ Gauss fit spectral line profile data base using the line width to distinguish between the diffuse molecular (as narrow line widths) and diffuse H I or WIM (as the broader line widths, corresponding to line wings in Figure 4). To analyze the diffuse gas we exclude all Gauss fit [C II] components with associated CO emission. Then we examine the velocity widths of the remaining Gaussian fitted components to separate the denser H_2 clouds from the diffuse gas. Figure 11 is a histogram plot of the number of [C II] spaxels as a function of line width for these [C II]-w/o-CO components. There is a narrow distribution of linewidths ($\Delta V < 7$ or 8 km s^{-1}) that peaks at ∼3 km s^{-1}. This line width range is characteristic of dense molecular clouds. However, there is a tail to the distribution with a peak ∼10 to 15 km s^{-1}. These broader line widths are similar to the spectral line "wings" shown in Figure 4 and can be interpreted as diffuse H I gas or WIM. Note this H_2 gas component is different from the CO-dark H_2 gas in the outer layers of CO clouds. Following Bolatto et al. (2013) here we refer to it as (CO-fant) diffuse H_2 gas. (There is some confusion in the literature as there is no agreed upon label for this component, and it is also referred to as CO-dark H_2 gas (Pineda et al. 2013), diffuse CO-dark H_2 gas (Langer et al. 2014b), "CO faint" molecular H_2 gas (Bolatto et al. 2013), and dark gas (Grenier et al. 2005; Wolfire et al. 2010).) Using the Gaussian fits for the [C II]-w/o-CO cloud components in the GOT C+ data base of Langer et al. (2014b), we estimate the sum of the [C II] intensities for (i) the narrow (< 8 km s^{-1}) velocity width components (seen in Figure 11) as a measure total intensity of the diffuse H_2 gas, (ii) the broader (> 8 km s^{-1}) velocity width components as a measure total intensity of diffuse atomic H I clouds and/or WIM gas, and (iii) all the Gauss fit components with or without CO as a measure of the total Galactic [C II] emission. Then we estimate the fraction of the Galactic [C II] emission in the diffuse H_2 gas and that in the atomic H I and/or WIM. (The results are also shown in the final summary in Figure 14.)

4.3.2. Spaxel data: How much of [C II]-w/o-CO is in H I gas?

In the [C II]-w/o-CO spaxels data it is difficult to separate the (CO-faint) diffuse H_2 gas from the diffuse H I or WIM, unlike in the Gauss fit data discussed above, where we identify individual features from their line widths. Here we take a different approach which starts by examining the amount of [C II] that we expect to arise from the H I gas and use this criterion to distinguish whether the source is truly diffuse H_2. The question, how much [C II] emission is expected in the H I clouds or the H I gas layers surrounding the molecular clouds, has been been above in Section 4.2. In brief, one uses the H I intensities to derive the column density N(H) and scales it by the fractional abundance of ionized carbon to derive the column density of +, N(+) as in Eq. 1. However, such estimates are highly model dependent as the C^+ excitation has a high critical density, ∼3100 cm^{-3} for atomic H, and a relatively large excitation energy, $\Delta E/k = 91.2$K. Therefore the emission intensity is very sensitive to both density and temperature, or equivalently gas pressure (see Langer et al. 2014b). Furthermore the uncertainty in metallicity used to derive the + column densities from scaling the H I column densities is also a factor.

We use Equation 1 (in Section 4.2) to estimate the [C II] emission, $I(CII)_{HI}$, that can arise in the H I clouds and or layers. In Figure 12(a) we plot the [C II] spaxel intensity against the H I spaxel intensity, I(H I), for all [C II]-w/o-CO detections within $R_G < R_\odot$. This scatter plot contains no indication of any correlation between the [C II] and H I intensities. In this plot we also show (by dashed lines) a model calculation of the $I([C\,II])_{HI}$ intensity as a function of H I intensity that is expected from the excitation of C^+ by the H I gas within each spaxel volume for three assumed gas pressures: P_1 =3000 K cm^{-3}, P_2 = 6000 K cm^{-3}, and $P_3 = 10^4$ K cm^{-3}. Langer et al. (2014b) discuss in detail the appropriate gas pressures to estimate the [C II] intensity in H I gas. The lower pressure P_1 is more realistic for a typical H I gas cloud in the solar neighborhood and P_2 is a maximum within the molecular ring (Wolfire et al. 2003; Pineda et al. 2013), while the highest pressure P_3, which is typical of dense molecular gas, seem very unlikely for the H I gas layers or clouds (Langer et al. 2014b).

If this model of emission in H I clouds is correct then, as can be seen in Figure 12(a), for the low pressure case, P_1, none of the spaxels have detectable [C II] from excitation by atomic hydrogen at the detection limit of the GOT C+ survey and all show [C II] excess above what is expected for excitation by H I (Figure 12b). If all the [C II] intensity comes from the H I gas we will not see any [C II] excess and the fraction of spaxels with excess [C II] will be zero. For the higher pressure, P_2, some spaxels should be detectable in [C II], but even for P_3 the majority of the H I spaxels are unobservable in [C II] at the sensitivity of the GOT C+ survey. We illustrate this result in another way by plotting the spaxel fractions with [C II] excess in each H I intensity bin in Figure 12(b). The [C II] excess are computed as the observed [C II] in each spaxel *minus* the [C II] intensity predicted for the H I intensity and assumed gas pressure. For the model with P_1 all have [C II] excess and therefore the spaxel fraction is one for all H I intensities. For pressures P_2 and P_3 the spaxel fraction with [C II] excess decreases for H I intensities beyond ∼ 250 and ∼ 150 K km s^{-1}, respectively. Even in the higher pressure cases only a small percentage of the spaxels have [C II] intensities that could be produced by + excited by atomic hydrogen.

What is the likelihood that we are underestimating the contribution to [C II] emission from H I if the observed H I intensities are beam diluted or if there are optical depth effects? If the H I is

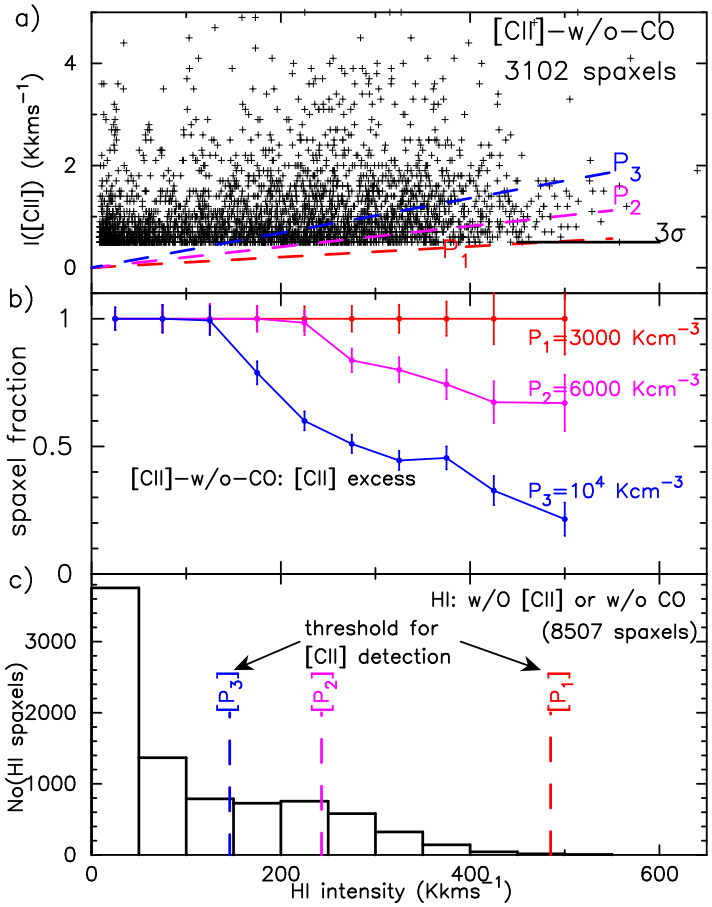

Fig. 12. Samples of diffuse [C II]-w/o-CO and H I without [C II] or CO for $R_G < R_\odot$. The gas pressures P_1, P_2, and P_3 in all panels (a) – (c) correspond to 3000, 6000, and 10^4 K cm^{-3}, respectively. (a) Scatter plot of [C II] intensities verses H I intensities for each spaxel. The dashed lines represent the [C II] intensities expected for H excitation of ϯ, corresponding to the H I intensity in each spaxel. The solid lines represent the 3-σ detection limit for [C II] in the 3 km s^{-1} wide spaxels. (b) Plot of the fraction of diffuse [C II] spaxels ([C II] without CO) in each H I intensity bin with [C II] intensities in excess of that expected for excitation in the H I clouds (see text). (c) Number distribution of H I spaxels without [C II] or CO plotted against H I intensity for the sample of diffuse H I spaxels without [C II] or CO. The dashed vertical lines indicate the minimum threshold H I intensity for detecting [C II] for pressure models P_1, P_2, and P_3.

not optically thin then N(H) is underestimated and correspondingly the true [C II] intensity is larger than those for the P_1 or P_2 curves in Figure 12(a). For example, Kolpak et al. (2002) estimate $\tau \sim 0.8$ to 1.4 for the inner Galactic regions between 4 and 8 kpc radius. Thus for a gas pressure P_1 (which is more realistic) combined with a factor of two intensity correction due to beam dilution or opacity, the emission from the H I gas doubles and will be identical to the predicted intensity shown for P_2 without beam dilution or optical depth corrections. However, we cannot expect beam dilution to be a significant effect much beyond this value, especially near the highest H I intensities, because it will produce extremely high values of H I intensities, resulting in very high column densities, N(H). However such high H I column densities are most likely to form molecular gas clouds, and will be detected as CO clouds with corresponding [C II] emission. Therefore the spaxel fractions with [C II] excess can be represented realistically by pressures between P_1 and P_2. Also, as shown below, P_3 seem unrealistic for the H I gas layers and we show it in Figure 12 to illustrate an extreme H I pressure.

We can also use our sample of 8507 diffuse H I clouds identified in the spaxels without [C II] or CO detections, to check for the consistency of the above estimates constraining the amount of [C II] emission from H excitation of ϯ (that is, the number of spaxels below our [C II] detection limit). This sample of spaxels clearly excludes any contamination from high density H_2 gas because none contain ^{12}CO. In Figure 12(c) are shown the intensity distribution of these H I spaxels along with the threshold limits for [C II] detection. In the case of P_1 all the spaxels have H I intensities below that required for detecting [C II] emission at the sensitivity of the GOT C+ survey. However, for gas pressures P_2 and P_3, GOT C+ should have detected many of these spaxels in [C II] emission. Thus in these clouds only the low pressure case, P_1, is consistent with the observations of H I but no [C II] detections. As seen in Figure 12(b), only a small fraction H I spaxels have intensities consistent with excitation by H while the majority have a large [C II] excess which cannot be accounted for by emission from H I gas alone. This excess could arise from (CO-faint) diffuse H_2 gas through excitation by H_2 or from the WIM excited by electrons.

4.3.3. [C II] fractions in (CO-faint) diffuse H_2 gas *versus* diffuse H I or the WIM

As seen in Figure 12(a) & (b) large number of spaxels in the [C II]-w/o-CO sample have a [C II] intensity excess above that predicted from excitation in H I layers and clouds, and this fact strongly favors the C^+ emission arising from the H_2 diffuse gas or WIM. Velusamy et al. (2012) suggested that excitation by electrons in the WIM accounts for a similar excess observed for the low surface brightness [C II] along the Scutum-Crux spiral tangency. Therefore, we use the spaxel [C II] intensity distributions to separate the emissions in the diffuse H_2 gas from that in the diffuse H I gas or the WIM. We examine the fraction of [C II] detections with and without CO as a function of [C II] intensity. The data are divided into [C II] intensity bins and in each bin the number of [C II] detections with and without CO are counted. In Figure 13(a) and (b) we plot the fraction of spaxels of [C II]-with-CO and [C II]-w/o-CO, respectively, as a function of the [C II] intensity. (The fraction [C II]-w/o-CO is just one minus that with CO shown in Figure 13a. However for convenience we plot it separately in Figure 13(b).) Here, the value of spaxel fraction for the [C II]-with-CO in a given [C II] intensity bin is defined as the ratio of the number of [C II] spaxels with CO detections to the total number of [C II] spaxels in the bin. Thus a fraction of unity will mean every [C II] detection has a CO counterpart and zero means none of the [C II] detections have CO.

As seen in Figure 13 the fraction of [C II] spaxels with and without CO show distinctly different relationships with the intensity of [C II], as denoted by the full and dashed lines. The [C II]-with-CO spaxels are more dominant at higher [C II] intensities, while the [C II]-w/o-CO detections are dominant at lower [C II] intensities. In the case of [C II]-with-CO it is not surprising because we already know (see Table 2) that this component is a dominant contributor to the Galactic [C II] emission. Of particular interest is the break in the slope of the dashed line near ~ 2.5 K km s^{-1}. This break identifies the following two populations: (i) a set of [C II] spaxels with a detection rate of [C II]-with-CO increasing rapidly toward low [C II] intensities, which we identify as diffuse H I or WIM gas components and (ii) a set of [C II] spaxels with a detection rate of [C II]-w/o-CO decreas-

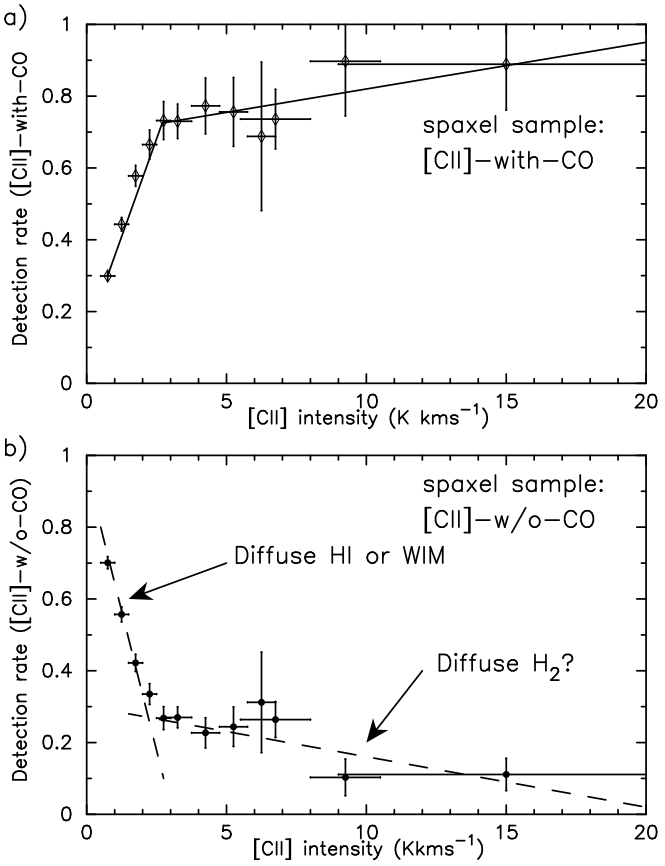

Fig. 13. The detection rates of [C II] gas components as a function of [C II] intensity: (a) Spaxel sample for [C II]-with-CO detection. (b) Spaxel sample for [C II]-w/o-CO detection. The error bars represent the widths of the [C II] intensity bins and the statistical error for each bin. The solid lines are approximate fits to the detection rates as a function [C II] intensity. The labels in the lower panel indicate the corresponding [C II] gas components.

ing slowly with increasing [C II] intensity, which we identify as a (CO-faint) diffuse H_2 gas component. Therefore we can interpret the spaxels in the long tail in Figure 13(b) at intensities > 2.5 K km s^{-1} as molecular gas and the lower intensity spaxels as the diffuse H I or WIM gas. Thus the break point in the [C II] intensity provides a useful marker for the sources of [C II] in these gas components and we estimate the [C II] gas fractions using the intensities above and below it. The fraction of [C II] in the diffuse H_2 gas without CO calculated from the spaxels is in good agreement with that estimated from the Gauss-fit analysis (Section 4.3.1).

In Figure 14 we show a flow diagram of the separation of [C II] emission into the different ISM gas components. As shown in Figure 14 from the GOT C+ spaxel analysis of [C II] detections, we obtain a [C II] intensity fraction of ∼ 27% from the diffuse H I and WIM components combined. Assuming a pressure of 3000 K cm^{-3} in the diffuse H I clouds (see panel (c) in Figure 12) and their observed H I intensities we estimate ∼ 6% of [C II] emission comes from the diffuse H I gas. We can then assign the remaining 21% of the [C II] intensity fraction to the WIM component. Thus in the diffuse ISM the WIM is more dominant as a source of [C II] emission than H I gas with a ratio of $[\mathrm{C\,II}]_{WIM}$ to $[\mathrm{C\,II}]_{\mathrm{HI}}$ ∼3. However, Pineda et al. (2013) calculated only 4% for the WIM emissivity at b=0°, using a model for the electron density distribution. It should be noted that this model only reproduces the electron density distribution over large scales and so underestimates the density due to neglecting the small filling factor (∼5% to 10%) for the WIM at b=0°. As the intensity is proportional to the density squared (Velusamy et al. 2012) times the filling factor, f, the emissivity $\propto f \times n(e)^2$ and Pineda et al. (2013) underestimates the actual WIM emissivity. Finally, we note that at the sensitivity of the GOT C+ survey we can only detect [C II] from the WIM in enhanced density regions, $n(e)$ > a few times the average electron density in the ISM such as those associated with the spiral arms (Velusamy et al. 2012), thus weighting our estimate of the fraction of [C II] from the WIM to more intense regions. Our result that a larger fraction of [C II] is in diffuse ISM is further corroborated by the broad z- scale distribution as discussed in Section 5.2. However, our estimate for the WIM fraction in [C II] is subject to the uncertainty in the gas pressure and the metalicity used for calculating the [C II] intensity in the diffuse H I gas (see Eq. 1).

4.4. Limit on [C II] in H I gas in spaxels with no [C II] detections

The analysis so far, and the [C II] fractions listed in Figure 14, only used the gas components with detected [C II] emission in their respective spaxels (above the 3-σ limit). For example, the 8507 H I spaxels in the inner Galaxy (see Figure 13(c)) are not included in the gas fractions as they all have [C II] intensities below the detection limit. Nevertheless their contributions to the total [C II] intensity and to gas fractions although small in each spaxel, may be significant in total. We can use the models discussed in Section 4.3.2 for + excitation by atomic H to estimate how much [C II] intensity will be expected from this sample of H I spaxels. From Figure 13(c) it is clear that only the gas pressure P_1 or less is appropriate for this sample. Using Equation 1 we estimate for these H I spaxels a total [C II] intensity of 928 K km s^{-1}, which amounts to ∼ 9% of the total [C II] intensity detected by GOT C+ in the inner Galaxy (see Table 2). However, we cannot estimate the corresponding [C II] emission in the WIM for the spaxels with [C II] intensities below the detection limit without detailed modeling of the WIM in each spaxel. We do not have any observational data, such as Emission Measures (EM) and/or electron densities, relevant for quantifying the electron excitation in each spaxel, unlike in the case of diffuse H I for which we could use the H I intensity for quantitative analysis of excitation in the H I gas. Therefore, for comparison between the [C II] fractions in H I and WIM we should regard our estimate for the WIM as a lower limit, which still makes the WIM a more dominant contributor to total [C II] emission than H I .

If we include the above limit on [C II] in the H I gas in the spaxels with no [C II] detection, the [C II] fraction in the diffuse H I gas is increased to ∼ 14.5% for cloud pressure P = 3000 K cm^{-3}. We estimate a similar amount, ∼12% of [C II] in H I gas associated with the denser molecular H_2 clouds (assuming a H I gas pressure P = 5000 K cm^{-3} and metallicity $\sim 2.2 \times 10^{-4}$ appropriate to the median spaxel radius $R_G \sim 5.5$ kpc). Thus our estimate of a total ∼27% for [C II] in H I gas is close to those derived by Pineda et al. (2013) for the Milky Way and Mookerjea et al. (2011) for M33. Therefore, we conclude that the total observed [C II] intensity originating from the H I gas (see Figure 14) is not the dominant source of the total of [C II] emission when compared to that from the H_2 gas or the WIM in the Galactic disk.

5. z–distribution of [C II] emission gas components

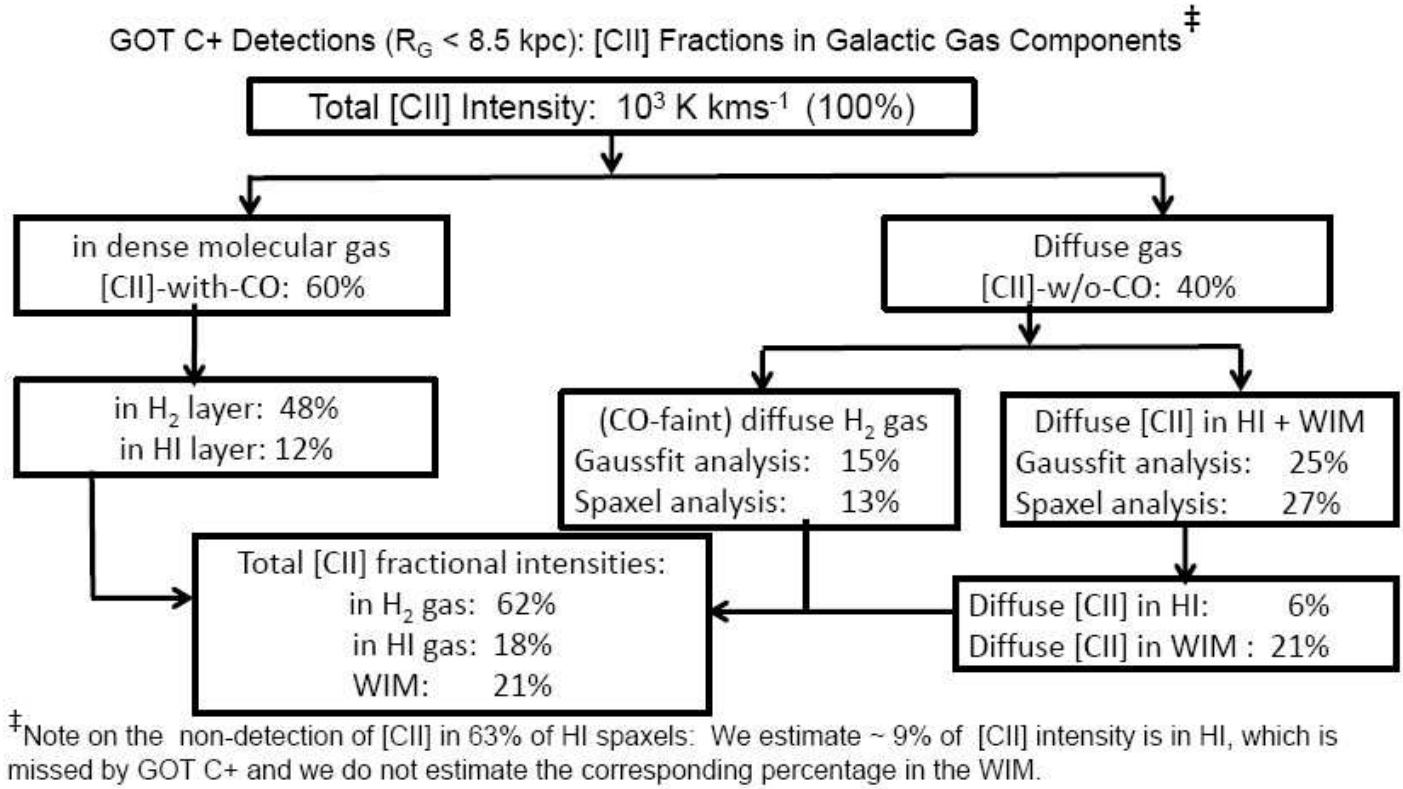
GOT C+ Detections (R_G < 8.5 kpc): [CII] Fractions in Galactic Gas Components‡
Total [CII] Intensity: 10^3 K kms^{-1} (100%)
in dense molecular gas
[CII]-with-CO: 60%
Diffuse gas
[CII]-w/o-CO: 40%
in H_2 layer: 48%
in HI layer: 12%
(CO-faint) diffuse H_2 gas
Gaussfit analysis: 15%
Spaxel analysis: 13%
Diffuse [CII] in HI + WIM
Gaussfit analysis: 25%
Spaxel analysis: 27%
Total [CII] fractional intensities:
in H_2 gas: 62%
in HI gas: 18%
WIM: 21%
Diffuse [CII] in HI: 6%
Diffuse [CII] in WIM : 21%
‡Note on the non-detection of [CII] in 63% of HI spaxels: We estimate ~ 9% of [CII] intensity is in HI, which is missed by GOT C+ and we do not estimate the corresponding percentage in the WIM.

Fig. 14. Summary of the Galactic [C II] emission fractions in different gas components in the inner Galaxy $R_G < R_\odot$. Note here we include only the estimated fraction in H I gas for the non-detections of [C II] in the H I spaxels but not the fraction from the WIM (see text in Section 4.4). We also note that the total [C II] gas fractions given here are estimated using the spaxel intensities alone and the estimates that include their z-scales are listed in Table 4

.

The scale height for ISM components in the disk is important for understanding the pressure and energetics of the gas, and for calculating the luminosity of the Galaxy in various gas tracers. In particular the determination of the [C II] luminosity is important because it is routinely used to trace galactic star formation. Whereas, those components traced by H I and CO are well established from large scale Galactic surveys, the gas traced by [C II] is not well established because the needed spectral line surveys of the 158-μm line have not, until recently, been available. Prior to GOT C+ all interpretations of the *z*-scale for [C II], were based solely on *b*–scans without distance information. These other large-scale Galactic plane surveys of [C II], namely, COBE (cf. Wright et al. 1991; Bennett et al. 1994), BIRT (Shibai et al. 1991), FILM onboard IRTS (Shibai et al. 1994; Makiuti et al. 2002), and BICE (Nakagawa et al. 1998) are spectrally unresolved. Consequently the *z*–distribution of the clouds traced by [C II] still remains not well characterized.

Only BICE, which surveyed the inner Galaxy (-350° < l < 25°), had sufficient latitudinal coverage with reasonable angular resolution, 15′, to determine the distribution in *b* up to the limit of their survey at $|b| = 3°$. FILM observed the [C II] distribution to larger values of *b* than BICE (Makiuti et al. 2002), but FILM only observed [C II] in a narrow strip along a great circle crossing the plane at $l = 50°$ (inner Galaxy) and 230° (outer Galaxy) and their latitudinal value was a strong function of longitude. In addition, the FILM data was smoothed to 1° to improve the signal to noise. Therefore, FILM mainly probed the local ISM (at 1 kpc $b = 5°$ corresponds to ~90 pc, above the bulk of the [C II] emission in the plane and is not likely representing high *z*–distances.) Without spectral resolution Nakagawa et al. (1998) were unable to assign a distance to the [C II] emission and derive a spatial profile. While the GOT C+ survey is spectrally resolved, it was limited to $|b| \leq 1°$, which is only ~150 pc at the distance to the Galactic center and so probes well the distribution only up to $z = \pm 150$ pc.

Recently, Langer et al. (2014a) estimated the average vertical [C II] *z*–scale height by "inverting" the BICE *b*–scan data using *a priori* knowledge of the radial distribution of Galactic [C II] emission at b=0° derived from GOT C+ data and showed that the total [C II] emission (from all gas components) has a broader *z*–distribution, FWHM ~172 pc, than CO (~110 pc), but narrower than H I (>230 pc). However, since the basic vertical [C II] data used in that analysis is the *b*–scan from BICE, it does not shed any light on the *z*–distribution of individual [C II] gas components, especially important for the diffuse [C II] arising from the CO-dark H_2 gas and the WIM, which are believed to have larger scale heights. GOT C+ surveyed [C II] sparsely in latitude at only b=0°, ±0.5°, and ±1.0°, and the approaches used in Pineda et al. (2013) and Langer et al. (2014b) only studied some of the global properties of Galactic [C II] emission as a function of Galactocentric radius. However, the spaxel analysis approach in this paper allows us to use the data in all latitudes *b*, combined with the V_{lsr}–Distance to each spaxel to derive the *z*–distributions.

To derive the *z*–distribution we resample the spaxels in 9 *z*-bins, from z = -160 pc to +160 pc, appropriate to each spaxel's observed latitude and V_{lsr}-Distance. In each *z*-bin we sum the (i) intensities of [C II], ^{12}CO, and ^{13}CO detections and (ii) inten-

sities of the [C II] gas components within each [C II] spaxel as described in Section 4. Because the sampling in b is heavily limited to only 5 discrete latitude values there is no uniformity of the sampling in z. For example nearly 1/3 of all spaxels populate the bin at z =0 pc while the rest are distributed irregularly among the other 8 z-bins. Therefore, as discussed in Section 4.1.2, to study the relative intensity distributions of each emission component as a function of z we need to "normalize" appropriately the sum of intensities in each z–bin. While, in principle, each spaxel (with fixed velocity width of 3 km s^{-1}) represents a Galactic volume element appropriate to its l, b, V_{lsr} and the beam area, it varies widely from spaxel to spaxel (especially near the tangencies) and is uncertain. Therefore, an absolute volume normalization will be very unreliable. Instead as discussed in Section 4.1.2 we use the number of H I spaxels in a given z–bin to represent a measure of the Galactic volume sampled within that z–bin and use this for normalization. As long as we have a sufficient number of H I spaxels in each z–bin we can derive a reasonable relative intensity z– distribution of CO, [C II] and its gas components.

Any attempt to study the z–distribution requires reasonably good distances to individual spaxels. Therefore, for this analysis, we use only the subset of the spaxels within R_G < 8.5 kpc for which there is no near– far–distance ambiguity (see Table 2). We also include the spaxels for which the near– far–distance ambiguity is resolved using H I absorption data (see Section 3.2.1). In addition, we include spaxels for which the near– and far–distances are within 2 kpc of each other (near the tangencies). In the latter case the error in the distances used to locate the emission from a spaxel could be as large as 1.0 kpc with a corresponding error in z of ~8 pc for $|b|$= 1.0°, which we believe is small enough to be included in our analysis. The number of spaxels used for determining the z–distribution are given in Table 2.

5.1. z-scale and FWHM distributions of [C II] and CO

To determine the z–distribution of [C II] we separated the spaxels into nine bins in z, as shown in the histogram at the bottom of the top panel in Figure 15. The width of the z–bins varies in order to have as many samples in each bin as possible, while at the same time providing sufficient coverage in z. Then we summed the spaxel intensities of each tracer within each z–bin. Note that we used only the intensities in the spaxels with 3-σ or better detections (using all the spaxels, including the ones with no signal, only introduces more noise). We then normalize the total intensity in each z–bin by dividing it by the number of H I spaxels in it (see histogram in Figure 15 top panel). As discussed above, the H I samples provide a good normalization for each z–bin. The error bars correspond to the 1-σ scatter in the spaxel intensities in each z–bin. Considering the availability of only a limited sampling of spectrally resolved data in b, we believe that this approach, the first ever attempt, provides good insight into the z–distribution for [C II] and the other tracers. Following Langer et al. (2014a), we assume a Gaussian profile to fit the emission distribution,

$$f(z) = f(z_c)e^{-0.5((z-z_c)/z_0)^2} \quad (2)$$

where z_0 is the scale height (where the full-width half-maximum, FWHM = $2(2\ln 2)^{0.5}z_0 = 2.35z_0$), z_c is an offset in the peak of the distribution, and $f(z_c)$ is the intensity at the peak in the distribution. For the z-scale analysis we use all detections of ^{12}CO and ^{13}CO with or without [C II], satisfying the criteria for R_G and distance as for [C II] and H I spaxels. We plot the distributions for the three gas tracers in Figure 15, for [C II], ^{12}CO, and ^{13}CO, and

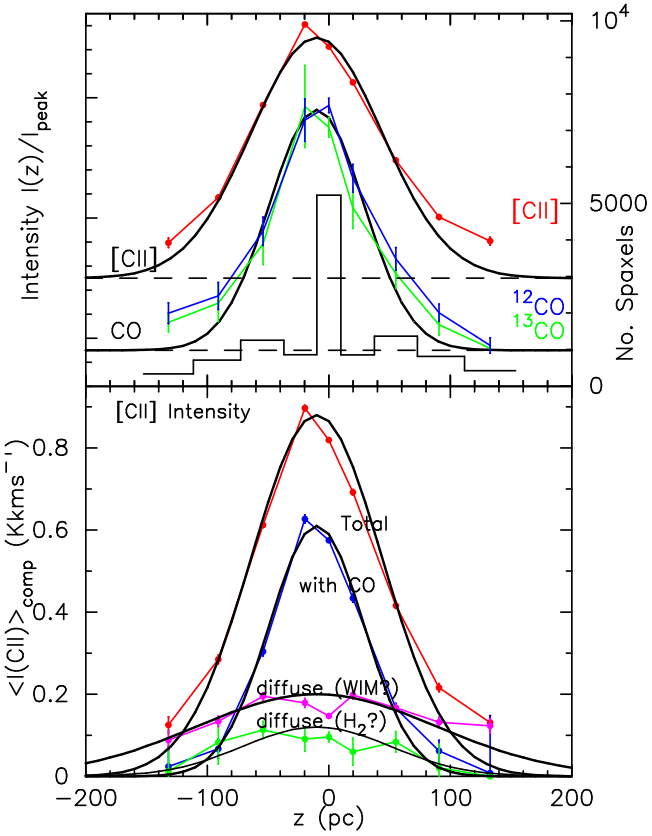

Fig. 15. The distributions of gas tracers as a function of z. (top panel) Comparison of average intensities of detections in each z–bin normalized to the peak: [C II] (red) and CO (blue and green). The total number of H I spaxels in each z–bin used to represent the "volume" sampled for averaging are shown by the histogram. (lower panel) Comparison of the average intensities of gas components of [C II] emission: total (red), with CO (blue), (CO-faint) diffuse H_2 (green), and diffuse (without CO) H I and WIM (magenta). In both panels the thick black lines represent Gaussian fits to the data (see fits in Table 3).

plot the Gaussians that fit the data. The Gauss fit parameters are given in Table 3. As can be seen in Figure 15 the Gaussians provide reasonable fits to the data. We are fairly confident of the fit to the [C II] distribution because the ^{12}CO and ^{13}CO in Figure 15 and their FWHM in Table 3 are consistent with the range of 60 – 140 pc for CO for R_G <$R_\odot$ derived from large scale Galactic CO surveys (cf. Sanders et al. 1984; Clemens et al. 1988). The H I distributions (not shown here) are also consistent with the multiscale height solution summarized by Dickey & Lockman (1990).

It can be seen in Figure 15 that the [C II] relative intensity (top panel) does not go to zero at z=±160 pc, and thus [C II] emission extends beyond this height. This result is consistent with the BICE and FILM observations of weak [C II] emission at values of $|b|$ > 1°, but the GOT C+ coverage is insufficient, as discussed above, to extend the distributions beyond this point. The z–distribution is important to calculate the [C II] luminosity of the Galaxy by combining the well sampled distribution in the plane with the vertical distribution (cf. Pineda et al. 2014). Furthermore, to calculate the luminosity of the Galaxy and study the dynamics of the different ISM components it is important to determine these individually rather than use an average value.

Table 3. *z*–distribution Gauss fit parameters:

Emission	peak‡	FWHM	z_c§	Intensity fractions integrated in *z*
	K km s^{-1}	(pc)	(pc)	(% of [C II]$_{total}$)
[C II]	0.9	179	10	100
^{12}CO	6.0	129	10	—
^{13}CO	0.9	129	10	—
[C II] gas components:				
[C II]-with-CO	0.61	129	10	48
Diffuse [C II]-w/o-CO:				
In CO-faint H_2	0.12	~202	10	14
In H I and WIM	0.20	~329	10	41

§z_c is an offset in the peak of the [C II] distribution
‡peak intensity in the *z*-bins (used for normalization)

5.2. *z*-scale of [C II] gas components

Our estimate for the *z*-scale FWHM for the total [C II] of 179 pc is in good agreement with the value of 172 pc calculated from the inversion of the BICE *b*–scan data by Langer et al. (2014a). However, in the analysis by Langer et al. (2014a) it was not possible to determine the scale heights of the separate gas components traced by [C II], because the [C II] data used in the *b*–scan is from BICE. Whereas, in the approach adopted here, we use only the GOT C+ data, and therefore, it allows us to separate the different gas components and their distributions. To derive their respective *z*–distributions we follow the procedure described in Section 5.1 for the total [C II] emission. We use the spaxels identified by their association with different tracers, as follows: (i) [C II]-with-CO as dense H_2 gas (see Section 4.2), (ii) bright diffuse [C II]-w/o-CO as the diffuse CO–faint H_2 gas (see Section 4.3.2), and (iii) low brightness diffuse [C II]-w/o-CO as diffuse H I or WIM (see Section 4.3.2). To estimate the *z*–scales we assemble the selected "labeled" spaxels in *z*–bins and find their average intensity in each bin. The results are shown in the lower panel in Figure 15. In this figure we plot the average intensities in each *z*–bin for the total [C II] and in its separate gas components. The approximate Gaussians to the z–distribution also are plotted in Figure 15 (lower panel). The Gaussian fit to the CO distribution in the top panel fits well the z–distribution of [C II]-with-CO. The error bars represent the 1-σ uncertainty estimated from the spectral noise in the spaxels. The "dips" in the intensities of the diffuse components correspond to spaxels at, or close to, the galactic plane ($b = 0°$) where the diffuse emission could be underestimated because of the overcrowding of the brighter [C II] velocity features (mostly seen along with CO). Nevertheless, the data in Figure 15 brings out clearly the *z*–extent of different [C II] components as indicated by the quality of the Gaussian fits. The Gaussian fit parameters are listed in Table 3 for the separate [C II] gas components. The Gaussian fits for the diffuse components in Figure 15 are indicative of their broader distribution, but the exact values of the FWHM should be used with caution given the small number of samples (see the histogram in Figure 15) for the *z*–bins available within the GOT C+ data and the uncertainties (~15 to 20 pc) in the *z*–distance estimates.

The vertical displacement of the peak of the emissions $z_c \sim$ 10 pc seem to fit all emissions and this may imply a simple displacement of the location of the Sun with respect to the Galactic plane. This result is consistent with the evidence of large-scale displacements of gas and young stars from a simple plane. (These displacements are significant as they are likely to be a consequence of the dynamical effects on disks in spiral galaxies (e.g., Lockman 1977; Matthews & Uson 2008; Widrow et al. 2012).)

Table 4. Overall Galactic [C II] emission fractions in different gas components in the inner Galaxy $R_G < R_\odot$, integrated over the inner Galactic disk, including the *z*-scales

ISM Gas component	[C II] intensity fraction[1]
[2][C II] fraction in dense H_2	48%
[2][C II] fraction in (CO-faint) diffuse H_2	14%
[3][C II] fraction in diffuse H I and WIM	41%
[C II] fraction in diffuse H I	10.5%
[C II] fraction in WIM	30.5%

[1]Includes only [C II] intensities above GOT C+ detection limit
[2]Ignoring the emission from H I layers in the H_2 clouds.
[3]Does not include emissions below GOT C+ detection limit

The [C II] sources associated with CO, have the narrowest distribution, FWHM = 129 pc, and, as expected, it agrees well with our value for CO emission because these are physically associated with each other, representing an identical population of CO spaxels with [C II] emission. This component makes the largest contribution to the total [C II] emission (at peak ~60%) but decreases sharply with *z*. In contrast the diffuse H I or WIM component has the largest extent (FWHM ~330 pc), as expected for [C II] emission from the WIM or diffuse H I and may be consistent with the weak emission observed by FILM at higher latitudes (cf. Makiuti et al. 2002). The scale height ~ 400 pc for the emission measure (EM) derived from the Wisconsin Hα Mapper (WHAM) data (cf. Gaensler et al. 2008) also suggests a larger *z*–distribution may be observed for the WIM component of the [C II] emission. The [C II] fraction in this diffuse component is ~22% near the plane of the disk and decreases slowly with *z*. Therefore, the intensity integrated over all *z* will be much larger and it will make a significant contribution to the Galactic [C II] luminosity. The (CO-faint) diffuse H_2 gas component has an intermediate *z*–distribution with a FWHM ~202 pc and its peak is ~13% of the total.

The (CO-faint) diffuse H_2 emission does not fit well with a Gaussian, instead its [C II] fraction stays nearly constant at a level of ~12% from $z \sim$ -100 pc to $\sim$ +60 pc and beyond that decreases faster. This result in particular is subject to the uncertainties due to having the fewest samplings of *z*–bins and is possibly underestimated because of overcrowding of bright [C II] features near the plane. Despite the smaller number of samples, we conclude with some confidence that the (CO-faint) diffuse H_2 gas traced by [C II] is significantly present from $z \sim$ -140 pc to $\sim$ +100 pc. In the case of the diffuse H_2 component it is possible that the flatness (or deficiency) near the plane, as indicated by data points in Figure 15 for the *z*–distribution, is real. Such a situation can be interpreted as a natural consequence of the timescales for cloud evolution in and out of the Galactic plane. Thus our results in Figure 15 is consistent with this difference and would imply that evolution from H I clouds to diffuse H_2 clouds and finally to CO molecular clouds is more rapid in the plane than at higher distances above the plane. Finally, we note that the distribution of the diffuse H I and/or WIM emission, having the largest FWHM, likely dominates the [C II] emission above the plane and is probably responsible to the high latitude emission seen by BICE and FILM.

We use the intensity for each gas component in Figure 15 and their respective Gauss fits in Table 3 to estimate the overall [C II] intensities and gas fractions integrated over the inner

Galactic disk both radially and vertically. This calculation is possible because the intensities at $z = z_c$ represent an average over the entire inner Galaxy $R_G < R_\odot$. We now know the form and extent of this emission in the vertical direction *z* from Equation (2). Then, by using the intensities and their FWHM listed in Table 3 we obtain the [C II] gas fractions averaged over the entire inner Galaxy including their *z*–scales. These estimates are summarized in Table 4. Although we do not fit *z*–distributions separately for the diffuse H I and WIM, in Table 4, we list their [C II] gas fractions averaged over the entire inner Galaxy, as estimated using the results in Section 4.3.3 for the ratio $[C\,II]_{WIM}$ to $[C\,II]_{HI}$ in the diffuse ISM (∼3), and assuming they have the same *z*-scales. However, our estimates are only relative to the averaged [C II] intensities and are not in absolute units representing a physical volume (as in pc^3). When given in absolute volume units this data can be readily compared with the brightness and luminosity in other galaxies. Nonetheless, these relative intensities (which includes the differences in their *z*-scale heights) as fractions of the total [C II] are still valuable for understanding the [C II] emission in the Galaxy as well as in external galaxies. If we have an estimate of the total [C II] luminosity of the Galaxy (e.g., Pineda et al. (2014) derived 10.1×10^{40} ergs s^{-1}) we can calculate the luminosity in each gas tracer for comparison to external galaxies by scaling the luminosity using the [C II] gas fractions in Table 4.

6. Summary

In this paper we show evidence of the prevalence of a diffuse [C II] emission component detectable in the HIFI position-velocity maps and in the line-wings of individual spectra. To provide a global perspective of distribution and origin of the gas components of [C II] emission in the Galaxy we made a comprehensive (3–km s^{-1} wide) spaxel by spaxel profile analysis of all GOT C+ survey and ancillary spectral line data toward the inner Galaxy ($R_G < R_\odot$), and characterized all the H I velocity features with and without [C II] detections. Our approach differs from previous analysis of the GOT C+ data base in that here we characterize the emission of [C II] and auxiliary CO, [C I], and H I in each spaxel along with kinematic distances derived from their V_{lsr}. We derive their 2-D distributions in the plane of the Galactic disk and in *z*. We find that the [C II] emission is correlated with the spiral arms in the Galaxy. We then analyze spaxel by spaxel the correlation of [C II] spaxel intensity to that of other gas tracers to identify the likely source of the diffuse [C II] emission.

The spaxels with [C II] detections were further divided into [C II]-with-CO and [C II]-w/o-CO. With this analysis we separated the diffuse [C II] component from that in the denser molecular H_2 gas and estimated the [C II] fraction in them (defined as the ratio of intensity in each gas component to the total [C II]). The diffuse [C II] emission was further classified by its possible identification with (i) [C II] in the diffuse molecular H_2 clouds (CO-faint) with a fraction ∼13% and (ii) with [C II] in diffuse H I clouds and the warm ionized medium (WIM) with a fraction ∼ 26%. We estimate that diffuse H I gas contributes ∼ 6% to diffuse [C II], thus the remainder (≥ 21%) comes from the WIM. The estimates of [C II] gas fractions derived using the spaxel intensities alone are given in Figure 14 and the estimates of the [C II] gas fractions that include their z–scales are listed in Table 4.

Our results are broadly consistent with those of Pineda et al. (2013) who calculated the [C II] emissivity in the plane for *b*=0°, except for the WIM. However, our determination for the WIM contribution comes directly from the data, whereas Pineda et al. (2013) calculated only 4% for the WIM emissivity for *b*=0°, using an electron density model which underestimates the WIM contribution to [C II] emission as discussed in Section 4.3.3. In the diffuse ISM we estimate the ratio $[C\,II]_{WIM}$ to $[C\,II]_{HI}$ ∼3, which makes the WIM the dominant source for diffuse [C II] observed with GOT C+. The large fraction of WIM contribution to [C II] is further corroborated by the extended *z*–scale of the diffuse [C II] component.

We estimate about 62% of the total [C II] intensity in the inner Galaxy is produced in H_2 gas. In other words, this fraction of [C II] intensity *traces* H_2 molecular gas clouds. Furthermore, it is possible, under extremely low $\frac{1}{3}$ excitation conditions such as at low kinetic temperatures (< 30K) and/or densities, in their C^+–H_2 layers, that the [C II] emission is not detected. In the GOT C+ survey not all CO detections have associated [C II] emission and thus a significant fraction of the Galactic H_2 gas is missed by [C II] as a H_2 gas tracer. Using CO as a H_2 gas tracer, we can estimate the fraction of H_2 molecular clouds missed by [C II] from the spaxels with CO and those with CO but no [C II] detections (see Table 2). A rough estimate of the fraction of the number of H_2 clouds missed by [C II] as a tracer is ∼ 38% suggesting a significantly large number of CO clouds are too cold to detect [C II] at the sensitivity of the GOT C+ survey.

We show that a comparison of CO with and without associated [C II] separates the warm and cold H_2 in the Galaxy. From their radial distributions the warm-H_2 gas fraction (∼ 0.6 to 0.7) peaking in the range 4 kpc < R_G < 7 kpc is consistent with the peaks in the star formation rate and star formation efficiency, and provides an important observational constraint on Galactic star formation.

One of the limitations in utilizing the GOT C+ data set for analyzing the *z*–distribution, is that it is a sparse survey covering longitudes from 0° to 360°, and only a few latitudes $|b| = 0°$, ±0.5°, and ±1.0°. A major difficulty in analyzing such a sparse data set is that not all of the Galactic volume is sampled equally, thus a quantitative analysis requires being able to normalize the sampling volumes throughout the Galaxy. We do not attempt to calculate a geometrical volume, which would be difficult to do, instead we have developed a normalization procedure or technique that uses the spaxels with H I emission to sample and measure an effective volume in the Galaxy. With this approach we are able, for the first time, to separate out the *z*–distribution of all ISM components traced by [C II]: (i) dense molecular H_2 clouds, associated with CO, having the narrowest distribution, FWHM = 129 pc similar to that of CO; (ii) the CO-faint diffuse molecular clouds being slightly broader, FWHM ∼ 202 pc; and, (iii) the broadest distribution is found for the diffuse [C II] arising from the atomic H I and/or ionized gas (WIM), with a FWHM ∼330 pc. All the fits and offsets are given in Table 3 along with a summary of the fraction of Galactic [C II] emission in these gas components. The *z*–distributions are subject to the uncertainties in resolving the near– far–distance ambiguity in the spaxel kinematical distances. Though these results are subject to the ambiguities in distances, the use of a large ensemble of spaxels in our statistical analysis reduces their effect on the result.

Calculating the Galactic [C II] gas fractions without the inclusion of *z*–scales tends to overestimate the fraction in dense molecular gas due to the dominance of molecular clouds in the plane (*b*=0°) while underestimating the diffuse [C II] components. Thus our results on the [C II] gas fractions, including their *z*-scales, provide a more robust estimate of the Galactic luminosity. Though these estimates of gas fraction are in relative intensities (which includes the differences in their *z*–scale heights) they are still valuable for understanding the [C II] emission in

the Galaxy as well as in external galaxies when used with the total [C II] luminosity (cf. Pineda et al. 2014). The GOT C+ data, publicly available in the *Herschel* archives provides a useful resource for any future work on + emission.

Acknowledgements. We thank the referee Dr. Jay Lockman for a careful reading of the manuscript and for constructive comments and suggestions. We thank the staffs of the ESA *Herschel* Science Centre and NASA *Herschel* Science Center, and the HIFI, Instrument Control Centre (ICC) for their help with the data reduction routines. This work was performed at the Jet Propulsion Laboratory, California Institute of Technology, under contract with the National Aeronautics and Space Administration.

References

Abel, N. P. 2006, MNRAS, 368, 1949
Bennett, C. L., Fixsen, D. J., Hinshaw, G., et al. 1994, ApJ, 434, 587
Bolatto, A. D., Wolfire, M., & Leroy, A. K. 2013, ARA&A, 51, 207
Braine, J., Gratier, P., Kramer, C., et al. 2012, A&A, 544, A55
Braine, J., Gratier, P., Kramer, C., et al. 2011, in IAU Symposium, Vol. 277, IAU Symposium, ed. C. Carignan, F. Combes, & K. C. Freeman, 63–66
Chengalur, J. N., Kanekar, N., & Roy, N. 2013, MNRAS, 432, 3074
Clemens, D. P., Sanders, D. B., & Scoville, N. Z. 1988, ApJ, 327, 139
Contursi, A., Kaufman, M. J., Helou, G., et al. 2002, AJ, 124, 751
Dame, T. M., Hartmann, D., & Thaddeus, P. 2001, ApJ, 547, 792
de Graauw, T., Helmich, F. P., Phillips, T. G., et al. 2010, A&A, 518, L6
Dickey, J. M. & Lockman, F. J. 1990, ARA&A, 28, 215
Englmaier, P., Pohl, M., & Bissantz, N. 2011, Memorie della Societa Astronomica Italiana Supplementi, 18, 199
Gaensler, B. M., Madsen, G. J., Chatterjee, S., & Mao, S. A. 2008, PASA, 25, 184
Goldsmith, P. F., Langer, W. D., Pineda, J. L., & Velusamy, T. 2012, ApJS, 203, 13
Gong, Y., Cooray, A., Silva, M., et al. 2012, ApJ, 745, 49
Grenier, I. A., Casandjian, J.-M., & Terrier, R. 2005, Science, 307, 1292
Heiles, C. 1994, ApJ, 436, 720
Jackson, J. M., Rathborne, J. M., Shah, R. Y., et al. 2006, ApJS, 163, 145
Johanson, A. K. & Kerton, C. R. 2009, AJ, 138, 1615
Kolpak, M. A., Jackson, J. M., Bania, T. M., & Dickey, J. M. 2002, ApJ, 578, 868
Langer, W. D., Pineda, J. L., & Velusamy, T. 2014a, A&A, 564, A101
Langer, W. D., Velusamy, T., Pineda, J. L., et al. 2010, A&A, 521, L17
Langer, W. D., Velusamy, T., Pineda, J. L., Willacy, K., & Goldsmith, P. F. 2014b, A&A, 561, A122
Levine, E. S., Blitz, L., & Heiles, C. 2006, Science, 312, 1773
Lockman, F. J. 1977, AJ, 82, 408
Makiuti, S., Shibai, H., Nakagawa, T., et al. 2002, A&A, 382, 600
Malhotra, S., Kaufman, M. J., Hollenbach, D., et al. 2001, ApJ, 561, 766
Mangum, J. G., Emerson, D. T., & Greisen, E. W. 2007, A&A, 474, 679
Matthews, L. D. & Uson, J. M. 2008, ApJ, 688, 237
McClure-Griffiths, N., Dickey, J., Gaensler, B., et al. 2005, ApJS, 158, 178
Meron, M. 1995, in http://www.astro.washington.edu/docs/idl/idllib/contrib/meron/
Mookerjea, B., Kramer, C., Buchbender, C., et al. 2011, A&A, 532, A152
Nakagawa, T., Doi, Y., Yui, Y. Y., et al. 1995, ApJ, 455, L35
Nakagawa, T., Yui, Y. Y., Doi, Y., et al. 1998, ApJS, 115, 259
Pilbratt, G. L., Riedinger, J. R., Passvogel, T., et al. 2010, A&A, 518, L1
Pineda, J. L., Langer, W. D., & Goldsmith, P. F. 2014, ArXiv e-prints, 1409.0537v1
Pineda, J. L., Langer, W. D., Velusamy, T., & Goldsmith, P. F. 2013, A&A, 554, A103
Pineda, J. L., Velusamy, T., Langer, W. D., et al. 2010, A&A, 521, L19
Pohl, M., Englmaier, P., & Bissantz, N. 2008, ApJ, 677, 283
Roman-Duval, J., Jackson, J. M., Heyer, M., et al. 2009, ApJ, 699, 1153
Sanders, D. B., Solomon, P. M., & Scoville, N. Z. 1984, ApJ, 276, 182
Shibai, H., Okuda, H., Nakagawa, T., et al. 1996, PASJ, 48, L127
Shibai, H., Okuda, H., Nakagawa, T., et al. 1991, ApJ, 374, 522
Shibai, H., Yui, M., Matsuhara, H., et al. 1994, ApJ, 428, 377
Stacey, G. J., Hailey-Dunsheath, S., Ferkinhoff, C., et al. 2010, ApJ, 724, 957
Steiman-Cameron, T. Y., Wolfire, M., & Hollenbach, D. 2010, ApJ, 722, 1460
Sternberg, A., Le Petit, F., Roueff, E., & Le Bourlot, J. 2014, ApJ, 790, 10
Stil, J. M., Taylor, A. R., Dickey, J. M., et al. 2006, AJ, 132, 1158
Vallée, J. P. 2008, AJ, 135, 1301
Velusamy, T., Langer, W. D., Pineda, J. L., & Goldsmith, P. F. 2012, A&A, 541, L10
Velusamy, T., Langer, W. D., Pineda, J. L., et al. 2010, A&A, 521, L18
Velusamy, T., Langer, W. D., Willacy, K., Pineda, J. L., & Goldsmith, P. F. 2013, in IAU Symposium, Vol. 292, IAU Symposium, 235–238
Widrow, L. M., Gardner, S., Yanny, B., Dodelson, S., & Chen, H.-Y. 2012, ApJ, 750, L41
Wiesenfeld, L. & Goldsmith, P. F. 2014, ApJ, 780, 183
Wolfire, M. G., Hollenbach, D., & McKee, C. F. 2010, ApJ, 716, 1191
Wolfire, M. G., McKee, C. F., Hollenbach, D., & Tielens, A. G. G. M. 2003, ApJ, 587, 278
Wright, E. L., Mather, J. C., Bennett, C. L., et al. 1991, ApJ, 381, 200